Loop currents in AV_3Sb_5 kagome metals: Multipolar and toroidal magnetic orders

Morten H. Christensen,[1,*] Turan Birol,[2] Brian M. Andersen,[1] and Rafael M. Fernandes[3]
[1]*Niels Bohr Institute, University of Copenhagen, 2100 Copenhagen, Denmark*
[2]*Department of Chemical Engineering and Materials Science, University of Minnesota, Minneapolis, Minnesota 55455, USA*
[3]*School of Physics and Astronomy, University of Minnesota, Minneapolis, Minnesota 55455, USA*

(Received 26 July 2022; revised 19 September 2022; accepted 29 September 2022; published 12 October 2022)

Experiments in the recently discovered vanadium-based kagome metals have suggested that their charge-ordered state displays not only bond distortions, characteristic of a "real" charge density wave (rCDW), but also time-reversal symmetry breaking, typical of loop currents described by an "imaginary" charge density wave (iCDW). Here, we combine density-functional theory, group theory, and phenomenological modeling to investigate the complex charge-ordered states that arise from interactions between the low-energy van Hove singularities present in the electronic structure of AV_3Sb_5. We find two broad classes of mixed iCDW-rCDW configurations: triple-**Q** iCDW, triple-**Q** rCDW order, dubbed 3**Q**-3**Q**, and double-**Q** iCDW, single-**Q** rCDW order, dubbed 2**Q**-1**Q**. Moreover, we identify seven different types of iCDW order, stemming from the different vanadium-orbital and kagome-sublattice structures of the two pairs of van Hove singularities present above and below the Fermi level. While the 2**Q**-1**Q** states trigger an orthorhombic distortion that breaks the threefold rotational symmetry of the kagome lattice, the 3**Q**-3**Q** states induce various types of subsidiary uniform magnetic orders, from conventional ferromagnetism to magnetic octupolar, magnetic toroidal, and even magnetic monopolar order. We show that these exotic orders display unique magnetostriction, magnetoelectric, and magnetoelectrostriction properties that can be probed experimentally to identify which iCDW state is realized in these compounds. We briefly discuss the impact of an out-of-plane modulation of the charge order and the interplay between these complex charge-ordered states and superconductivity.

DOI: 10.1103/PhysRevB.106.144504

I. INTRODUCTION

Systems in which electronic correlations and nontrivial topology are simultaneously present are of major interest for the condensed matter community. The kagome lattice [1] offers a promising platform to realize these phenomena [2], as its electronic structure exhibits Dirac cones [3–5], flat bands [6,7], and van Hove singularities [8]. Hence, the recent discovery of a new family of superconducting (SC) kagome materials [9], AV_3Sb_5 (A = K, Rb, Cs), with $T_c \sim$ 2 K depending on the alkali atom [10–12], was met with great enthusiasm by the community [2,13–15]. The nature of the SC state remains widely debated: While experiments have reported both nodeless [16–20] and nodal behavior [21,22], theoretical models have proposed unconventional chiral d-wave and f-wave states [23–26]. More exotic SC phenomena have also been discussed, motivated by intriguing data, including a time-reversal symmetry-breaking pairing state [21,27–29], a pair density-wave [19], and charge-4e and charge-6e condensates [30].

Superconductivity in these materials, however, emerges inside a charge density wave (CDW) state, which onsets at $T_{CDW} \sim 100$ K [9,31]. Importantly, T_{CDW} and T_c anticorrelate as a function of pressure, uniaxial stress, and doping [32–35]. Therefore, to achieve a complete description of the SC phase, much of the experimental and theoretical research has focused on elucidating the properties of the charge-ordered state [8,19,27,28,36–60]. It is well established that the CDW leads to a 2×2 increase of the unit cell in the (a, b) plane [37], whereas along the crystallographic c axis the increase can be a factor of 1, 2, or 4 depending on the alkali atom, pressure, and temperature [31,41,44,48,61]. The threefold rotational symmetry of the lattice has also been reported to be broken at either T_{CDW} or well below the onset of CDW order [38,46,47,62,63]. Consistent with these observations, a second CDW phase has been observed to emerge in the phase diagram of certain compounds [29,61]. These results are compatible with a scenario in which multiple CDW states with wave vectors sharing the same in-plane components $(1/2, 1/2, Q_z)$ have comparable energy scales, as suggested by first-principles calculations [39,53,54,60].

The most surprising property of the CDW state, which makes it stand out compared to other CDW phases like those seen in metallic chalcogenides [64–67], is that it appears to break time-reversal symmetry, as reported by scanning tunneling microscopy (STM), muon spin resonance (μSR), and magneto-optical Kerr effect (MOKE) measurements [21,27,28,37,49,63,68]. A time-reversal symmetry-broken charge order has a natural interpretation in terms of periodic patterns of loop currents [69,70], reminiscent of the Haldane model for the quantum Hall effect [71]. Theoretically, these loop currents are described in terms of an "imaginary" CDW (iCDW) order parameter—to be contrasted with a "real" CDW (rCDW) order parameter describing bond distortions or charge variations at the lattice sites [70,72,73].

*mchriste@nbi.ku.dk

The existence of such loop currents is further supported by recent measurements of field-tuned chiral transport in CsV_3Sb_5 [74]. Previous work has shown that the combination of van Hove singularities (vHs) in the electronic dispersion and electron-electron interactions can promote such iCDW states [50–52]. Importantly, the symmetries of the kagome lattice generally entangle the iCDW and rCDW order parameters, creating complex charge-order patterns that display both loop currents and bond distortions [50,51,57]. Moreover, while the symmetry of the rCDW order parameter can be inferred from first-principles and recent phonon spectroscopy data [39,48,53,54,60], the symmetry of the iCDW state remains unsettled. Thus, distinguishing the unique signatures of the many allowed mixed iCDW-rCDW configurations is paramount to establish the origin of the charge-order instability and, ultimately, the properties of the normal state from which superconductivity emerges.

In this paper, we combine group theory, first-principles calculations, and phenomenology to classify the viable iCDW-rCDW configurations that arise from interactions between the low-energy electronic states associated with the vHs of AV_3Sb_5, which are located near the three symmetry-equivalent M points of the Brillouin zone (BZ). The key point is that there are multiple low-energy vHs—a pair of points above and a pair of points below the Fermi energy—with different vanadium orbital characters (d_{z^2}, d_{xz}, and d_{yz}) and distinct vanadium sublattice polarization (p type, corresponding to "pure" sublattice polarization, and m type, corresponding to "mixed" sublattice polarization [52,75]). From this rich landscape, we find various intraorbital and interorbital loop-current patterns, resulting in seven different types of iCDW order parameters, corresponding to seven different irreducible representations (irreps) of the space group. In the presence of spin-orbit coupling, an iCDW transition necessarily triggers a spin density wave (SDW) at the same wave vectors [76], which could in principle be probed by neutron scattering. By using group theory, we show that the most natural way to understand the SDW is in terms of magnetic moments on the in-plane Sb ions, whose directions (i.e., in-plane versus out-of-plane) depend on the orbital character of the iCDW order.

Remarkably, all cases considered here display the same iCDW-rCDW coupled Landau free energy. By analyzing the minima of this free energy, we find two general types of mixed iCDW-rCDW configurations for each of the seven iCDW order parameters. The first one is a 3**Q**-3**Q** configuration, in which the iCDW and rCDW order parameters both condense at the three distinct M wave vectors. The second one is a 2**Q**-1**Q** configuration, where the iCDW order parameter condenses at two distinct M wave vectors and the rCDW order parameter condenses at the remaining M wave vector. We note that, while the first type of mixed iCDW-rCDW configuration was discussed in Ref. [50] for the case of intraorbital iCDW order, here we also consider interorbital iCDW states as well as the 2**Q**-1**Q** configuration.

Given the challenges in directly probing loop currents experimentally, we also analyze the experimental manifestations of these different mixed iCDW-rCDW configurations. Besides the finite-q magnetism (i.e., SDW) triggered by the iCDW alone, the mixed iCDW-rCDW phases with 3**Q**-3**Q** order also display uniform (i.e., $q = 0$) magnetism. In the case of an iCDW involving the same vHs, the latter corresponds to ferromagnetic (FM) order with spins on the Sb sites pointing out of the plane. Conversely, in the case of iCDW involving different vHs, the 3**Q**-3**Q** mixed phase displays no net dipolar moment. Instead, we find that it gives rise to exotic types of uniform magnetism, such as octupolar, toroidal, and even monopolar magnetic order. We show that each of these subsidiary orders couples uniquely to a combination of external magnetic, electric, and strain fields, displaying characteristic magnetostriction and multiferroic properties that can be detected experimentally.

As for the 2**Q**-1**Q** mixed iCDW-rCDW configurations, although they do not display any type of uniform magnetic order, they spontaneously break the threefold rotational symmetry of the lattice and give rise to an orthorhombic distortion. This happens regardless of whether the iCDW is made out of electronic states from the same or different vHs. Finally, we extend our analysis to the case of an iCDW modulated along the c axis and discuss the broad implications of our results for the identification of the complex charge-order patterns realized in the AV_3Sb_5 compounds, as well as their interplay with superconductivity.

This paper is organized as follows: In Sec. II, we analyze the orbital and sublattice characters of the Bloch states at the van Hove singularities at the M point and classify these according to the irreps of the $P6/mmm$ space group. The candidate charge orders that can arise from the occupied vHs Bloch states are introduced in Sec. III. These come in both intra- (Sec. III A) and interorbital (Sec. III B) varieties, each giving rise to distinct types of charge order with different properties. In Sec. IV, we introduce the coupled Landau free energy of real and imaginary charge orders and argue that a mixed configuration—either a 3**Q**-3**Q** or a 2**Q**-1**Q** phase—is generally favored. Section V presents the experimental signatures of the mixed charge ordered phases. In Sec. VI, we discuss the impact of the unoccupied vHs Bloch states. Finally, Sec. VII contains our conclusions. Additional details of the first-principles calculations are show in Appendix A, whereas details of the classification of the Bloch states in terms of space group irreps are included in Appendix B.

II. ORBITAL AND SUBLATTICE CHARACTER OF THE VAN HOVE SINGULARITIES

We start by employing group theory to elucidate the symmetry properties of the low-energy electronic states near the vHs. Interactions involving these states have been proposed to give rise to different types of CDW and SC order [50–52]. Note that a similar type of analysis was previously done in Ref. [50]. In this paper, besides recovering some of the results of Ref. [50], we consider additional types of iCDW order and mixed iCDW-rCDW configurations.

At room temperature, the AV_3Sb_5 compounds belong to the crystallographic space group $P6/mmm$, which has a simple hexagonal BZ. In Fig. 1(a) we illustrate the vanadium atoms of the kagome layer, with the three distinct vanadium sublattice sites highlighted by different colors. The vHs correspond to the saddle points of the band dispersion located at the M points of the BZ. There are three symmetry-related M

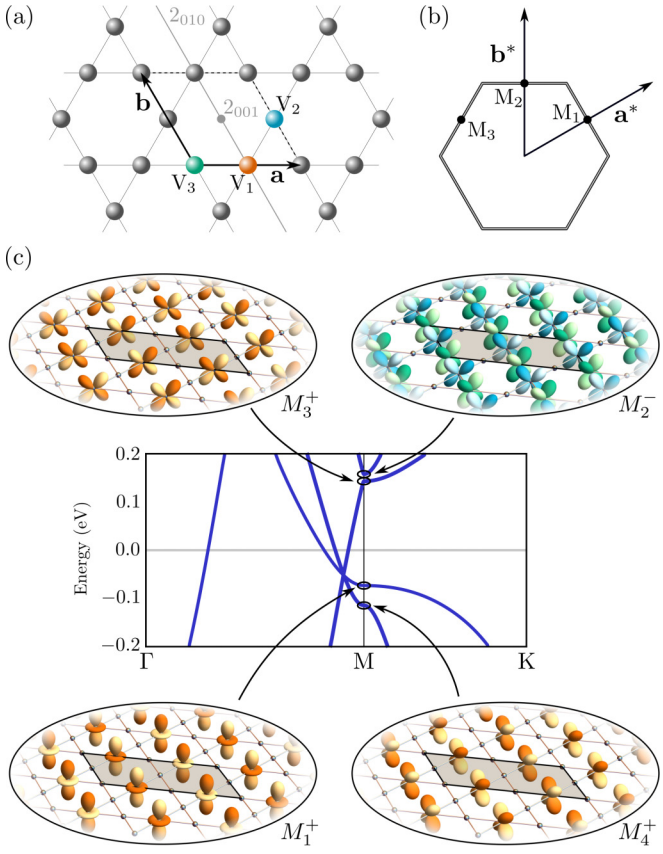

FIG. 1. (a) Vanadium kagome layer of AV_3Sb_5 including the choice of lattice vectors, **a** and **b**, and the three distinct V sublattice sites, V_1, V_2, and V_3 (in orange, blue, and green, respectively). The generators of D_{2h}, which is the V site-symmetry point group, are denoted in gray and consist of two axes of twofold rotations, 2_{001} and 2_{010}, as well as inversion. (b) Hexagonal BZ of the unit cell shown in (a) with reciprocal lattice vectors $\mathbf{a}^*$ and $\mathbf{b}^*$ and the three symmetry-related M points denoted by M_1, M_2, and M_3. (c) Band structure along the $\Gamma - M - K$ direction obtained from DFT calculations for CsV_3Sb_5 and the associated Bloch states near M_1. Four vHs (two occupied and two unoccupied) arise from the saddle points at the M point, whose Bloch states are dominated by the d_{z^2}, d_{xz}, and d_{yz} V orbitals (insets). Note that the sign of each orbital is modulated along M_1. The extended 2×1 unit cell is denoted by the gray rectangle in the insets. At three of the M_1 vHs, the Bloch states are composed of orbitals located at V_1 (p-type vHs). The Bloch state at the fourth vHs, which is farthest from the Fermi level, is composed of orbitals located at the V_2 and V_3 sites (m-type vHs). The irreps of each Bloch state are indicated in the insets.

points, which we denote by M_i and describe by the momenta $\mathbf{Q}_i = (\pm\pi, \frac{\pi}{\sqrt{3}}, 0), (0, \frac{2\pi}{\sqrt{3}}, 0)$, with $i = 1, 2, 3$ [see Fig. 1(b)]. As shown in Fig. 1(c), electronic structure calculations using density functional theory (DFT) predict two vHs below the Fermi level and two vHs above the Fermi level at the M point in the AV_3Sb_5 materials [8,9,25,37,53,77,78]. This is consistent with results from angle-resolved photo-emission spectroscopy (ARPES) [8,79]. We note that the band dispersions associated with the two vHs located above the Fermi level undergo an avoided crossing before the M point is reached, which masks the saddle points. While the electronic structure shown in Fig. 1(c) is obtained for CsV_3Sb_5, the general features are valid for all the AV_3Sb_5 compounds. In particular, the analysis of the wave functions presented below does not depend on the specific compound in question.

TABLE I. Characters of the irreps of the little group of the M_1 point. We only list the characters for the three generators of the little group, and these irreps correspond to the space group irreps by the same name. Note that even though the little group irreps are one dimensional, the corresponding space group irreps are three dimensional, because the star of M has three distinct wave vectors.

	2_{001}	2_{010}	$\bar{1}$
$M_1^\pm$	+1	+1	±1
$M_2^\pm$	+1	−1	±1
$M_3^\pm$	−1	+1	±1
$M_4^\pm$	−1	−1	±1

Let us first analyze the wave functions of the vHs below the Fermi level, i.e., the occupied vHs. The key result is that these saddle points have atomic contributions from only one of the three vanadium atoms in the unit cell. In other words, labeling the three distinct V atoms in real space by V_i [Fig. 1(a)], the saddle points at a particular M_i point in momentum space below the Fermi level [Fig. 1(b)] arise from the dispersion of orbitals at V_i only. Thus, in the notation of, e.g., Refs. [8,75], both saddle points correspond to a p-type (i.e., "pure") vHs. To highlight the fact that these saddle points are located below the Fermi level, here we denote them as p_--type vHs.

The main difference between these two vHs is that they have different vanadium orbital characters. To show that, we classify them in terms of the irreducible representations (irrep) of the space group $P6/mmm$ at the M point, which are labeled by $M_\alpha^\pm$ with $\alpha = 1, \ldots, 4$ (see also Table I). Note that italic M refers to the irrep whereas regular M refers to the BZ point. While the state at the occupied saddle point at M closest to (but below) the Fermi level transforms as the M_1^+ irrep, the state at the lower one transforms as the M_4^+ irrep. To connect these irreps to the V d orbitals, we note that the latter can be classified according to the irreps of the site-symmetry point group of the V site, which is D_{2h}. Considering first the fully symmetric A_g orbitals, corresponding to the d_{z^2} and $d_{x^2-y^2}$ orbitals, we can use group theory to establish the irreps of the bands induced by them [80],

$$A_g \uparrow P6/mmm \sim M_1^+ \oplus M_3^- \oplus M_4^- . \tag{1}$$

In this notation, the z axis is parallel to the crystallographic c direction, whereas the x axis can be chosen parallel or perpendicular to the b direction for V_1. Note that even though all three vanadium atoms are symmetry equivalent, they each have a different local coordinate system that differ by a rotation around the z axis. Hereafter, we use local coordinate axes such that the x axes point towards the center of the hexagon formed by vanadium atoms. Therefore, from Eq. (1), we conclude that the occupied saddle point nearest to the Fermi level at the M point has A_g orbital character. Our DFT calculations (details in Appendix A) reveal that the d_{z^2} orbital provides the leading contribution, whereas $d_{x^2-y^2}$ gives the subleading one. The fact that the orbitals of only one of the three V atoms

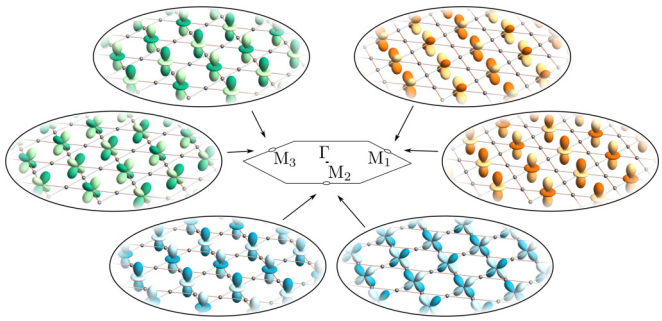

FIG. 2. Orbital and V-sublattice character of the Bloch states describing the two *occupied* vHs closest to (but below) the Fermi level at each of the three M points. The phase of the orbital is modulated along a different direction depending on the BZ point, M_1, M_2, and M_3. The orbital weight for a given M point is concentrated on a distinct V site resulting in *p*-type vHs. Moreover, the V d_{xz} orbital is defined with respect to a local coordinate system, as explained in the main text.

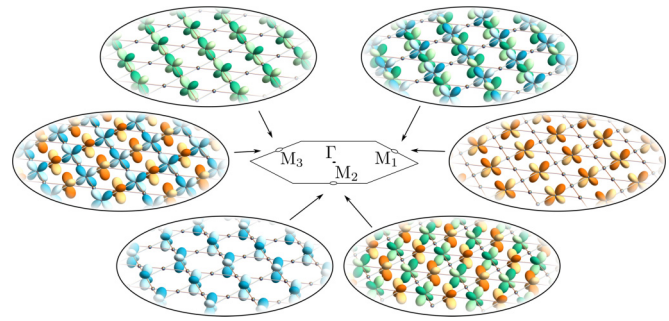

FIG. 3. Orbital and V-sublattice character of the Bloch states describing the two *unoccupied* vHs above the Fermi level at each of the three M points. The phases of the orbitals are modulated along a different direction depending on the BZ point, M_1, M_2, and M_3. The d_{yz} orbitals contributing to the Bloch state associated with the unoccupied vHs closer to the Fermi level arise from a single V site. This is similar to the situation in Fig. 2, thus resulting in a *p*-type vHs. On the other hand, the d_{xz} orbitals contributing to the other unoccupied vHs arise from the other two V sites, leading to an *m*-type vHs.

contributes to this saddle point is illustrated in Fig. 1(c), where we show for simplicity only the dominant d_{z^2} orbital. Note that the appearance of only d_{z^2} and $d_{x^2-y^2}$ as orbital states is a consequence of using a local coordinate system for each V atom. As the local coordinate system is different at each V atom, the lobes of the $d_{x^2-y^2}$ states are also oriented differently at each site. Hence, the $d_{x^2-y^2}$ states cannot be defined with respect to a global coordinate system. In this case, the states at two of the V atoms would become superpositions of $d_{x^2-y^2}$ and d_{xy}, defined with respect to the global coordinate system, in addition to the dominant d_{z^2} orbital.

The second occupied saddle point at M closest to the Fermi level arises from a B_{2g} orbital (or B_{3g} depending on the choice of the x axis), which corresponds to the d_{xz} orbital in the aforementioned local coordinate system. If a single global coordinate system is used for all three vanadium atoms in the unit cell, then the B_{2g} orbitals would correspond to a linear superposition of d_{xz} and d_{yz} orbitals (see Appendix B for details). In a manner similar to Eq. (1), the B_{2g} orbital also induces three bands near M, one of which transforms precisely as M_4^+. This band also has a particularly simple wave function with contributions from only a single V atom in the unit cell, as shown in Fig. 1(c).

Figure 2 summarizes the main results of the group theory analysis performed in this section for the Bloch states of the occupied saddle points at the three different M points that are closest to (but below) the Fermi level. At each M point, the wave functions of a given saddle point are located on different V atoms. Moreover, the spectral weight of each of the two vHs at a given M point is dominated by a different type of V d orbital, denoted here by A_g (d_{z^2}, $d_{x^2-y^2}$) and B_{2g} (d_{xz}). As we discuss in Sec. III, the different symmetry properties of the two occupied van Hove singularities have important implications for the types of charge order that can arise in the AV_3Sb_5 kagome metals.

We now move to the two unoccupied vHs whose energies are above the Fermi energy. While they appear more distant from the Fermi level than the pair of occupied vHs, the relative energy difference is small enough that it is prudent to also consider them in the analysis. The unoccupied vHs closest to the Fermi level has the same *p*-type structure as the occupied vHs—in this case, we denote it p_+-type to emphasize that it is located above the Fermi level. As illustrated in Fig. 1(c), its wave function is dominated by the (local) d_{yz} orbitals from a single vanadium site. In contrast to the occupied vHs, the lobes of these B_{3g} orbitals point towards the V-V bonds. As a result, this Bloch state transforms as a different irrep than the two occupied ones, namely M_3^+.

The wave function of the unoccupied vHs that is farthest from the Fermi energy in Fig. 1 has a completely different sublattice structure from the other vHs discussed so far. As shown in Fig. 1(c), this wave function is also dominated by d_{xz} orbitals in the local coordinate system, but from the other two vanadium sites. More specifically, at the M_i point, the vHs wave function has sublattice contributions from the vanadium sites V_j and V_l, where (i, j, l) is a permutation of (1,2,3). Using the nomenclature of Refs. [8,75], this is an *m*-type (i.e., "mixed") vHs; since there is no *m*-type vHs below the Fermi energy in our low-energy model, we do not include the subscript $+$. More importantly, the Bloch state of this *m*-type vHs transforms as the M_2^- irrep of the space group. The minus sign in the superscript is a consequence of the fact that this combination of orbitals is odd under an inversion operation with respect to the center of the hexagon formed by V sites. As we will discuss later in Sec. VI, the distinct symmetry properties of this particular vHs have crucial implications for the types of iCDW that it can generate. In Fig. 3, we summarize the orbital and sublattice character of the Bloch states corresponding to the pair of unoccupied vHs.

III. CANDIDATE CHARGE ORDERS: OCCUPIED VAN HOVE SINGULARITIES

Because they are the ones closest to the Fermi level, we start our analysis by considering first only the two occupied p_--type vHs at the M point. These are made out of different vanadium orbitals from the same V sublattice. The role of

the unoccupied vHs will be considered in Sec. VI. In our approach, we depart from the electronic Bloch states obtained in Sec. II, classify the possible intra- and interorbital charge order parameters, and discuss their real-space realizations. We note that a similar analysis was performed in Ref. [50] considering only one of the saddle points.

Our focus is on the rCDW and iCDW order parameters with wave vector $\mathbf{Q}_{M_i}$, which we denote by N_i and Φ_i, respectively, following the notation of Ref. [50]. Importantly, these order parameters must transform as one of the $M_\alpha^\pm$ irreps of the $P6/mmm$ space group. Because the irreps associated with rCDW and iCDW transform in different ways under the time reversal operation (even and odd, respectively), they are distinct order parameters with different symmetry properties. Formally, the irreps $M_\alpha^\pm$ are all real and three dimensional, arising from the three vectors in the star of M. Hence, order parameters transforming as these irreps have three components. As a consequence, the rCDW and iCDW order parameters are independent of each other, and do not transform as the real and imaginary parts of a single complex CDW order parameter as this would have six components.

A. Intraorbital rCDW and iCDW

Let $c^\dagger_{\mathbf{k}\sigma}$ and $d^\dagger_{\mathbf{k}\sigma}$ denote the creation operator of an energy eigenstate near the occupied M_1^+ and M_4^+ vHs, respectively. Here, $\mathbf{k}$ denotes momentum and σ spin. Because the M_1^+ and M_4^+ saddle points are composed of different types of orbitals (A_g and B_{2g}, respectively), the allowed intraorbital charge order parameters with wave vector $\mathbf{Q}_i$ are those that combine fermions of the same species, i.e., fermions from the same type of saddle point at two different M points.

As discussed above, there are two independent types of charge order: rCDW and iCDW. The intraorbital rCDW order parameters are given by (see also Ref. [50])

$$N_i^c = \sum_{\mathbf{k}\sigma} \langle c^\dagger_{\mathbf{k}+\mathbf{Q}_j\sigma} c_{\mathbf{k}+\mathbf{Q}_l\sigma} + \text{H.c.}\rangle, \tag{2}$$

$$N_i^d = \sum_{\mathbf{k}\sigma} \langle d^\dagger_{\mathbf{k}+\mathbf{Q}_j\sigma} d_{\mathbf{k}+\mathbf{Q}_l\sigma} + \text{H.c.}\rangle. \tag{3}$$

In the equations above and in all definitions of the CDW order parameters in this paper, we use the convention that (i, j, l) is a permutation of (1,2,3). The subscript $i = 1, 2, 3$ denotes the three components of the order parameter, associated with the three wave vectors $\mathbf{Q}_{M_i}$ in the star of M. Similarly, the iCDW order parameters are

$$\Phi_i^c = i \sum_{\mathbf{k}\sigma} \langle c^\dagger_{\mathbf{k}+\mathbf{Q}_j\sigma} c_{\mathbf{k}+\mathbf{Q}_l\sigma} - \text{H.c.}\rangle, \tag{4}$$

$$\Phi_i^d = i \sum_{\mathbf{k}\sigma} \langle d^\dagger_{\mathbf{k}+\mathbf{Q}_j\sigma} d_{\mathbf{k}+\mathbf{Q}_l\sigma} - \text{H.c.}\rangle. \tag{5}$$

Note that, despite the "imaginary" denomination, the iCDW order parameter is real valued. As we emphasize below, the distinction between rCDW and iCDW stems from the fact that the first corresponds to charge disproportionation at sites and/or bonds and the second, to loop currents.

The symmetry properties of the order parameters N_i^μ and Φ_i^μ, with $\mu = c, d$, can be directly obtained from the symmetry properties of the creation and annihilation operators. The latter, in turn, are determined by the Bloch states derived in Sec. II, which transform as either M_1^+ (for $\mu = c$ fermions) or M_4^+ (for $\mu = d$ fermions). Details of the derivation can be found in Appendix B. For the rCDW case, we find that both intraorbital order parameters N_i^μ transform as the M_1^+ irrep of the $P6/mmm$ group. Since the point symmetry part of the little group at M is D_{2h}, this means that each of the three components of N_i^μ transforms trivially under the operations of D_{2h} (with rotation axes aligned differently for each wave vector), as shown in Table I—although they break the translational symmetry along the ith direction. Such an rCDW order corresponds to V-V bond distortions, and is consistent with experimental evidence for the presence of an M_1^+ lattice distortion concomitant with the onset of charge order [39,40,48]. The triple-$\mathbf{Q}$ rCDW order, which corresponds to the condensation of all three components N_i^μ with equal amplitudes, gives rise to either the star-of-David or trihexagonal bond-order configurations depending on the sign of $N_1N_2N_3$ [54].

As for the iCDW case, we find that the order parameters Φ_i^μ transform as the mM_2^+ irrep of $P6/mmm$. Here, m denotes the fact that the irrep is odd under time-reversal symmetry. Additionally, it breaks the lattice translational symmetry and the in-plane twofold lattice rotation axis, as indicated in Table I. In Fig. 4(b), we illustrate Φ_1^c as hopping between d_{z^2} orbitals centered on the V_2 and V_3 sites. The different colors denote a relative phase of $\pi/2$ between orbitals on neighboring V atoms; it is such a phase difference that defines the current direction. In this particular case, the translational symmetry is broken along the crystallographic a axis, as expected for the wave vector $\mathbf{Q}_1$. A similar current pattern involving the B_{2g} orbitals also exists simultaneously to the pattern shown in Fig. 4(b). Indeed, since Φ_1^c and Φ_1^d transform as the same irrep, one order necessarily triggers the other one.

For a single-$\mathbf{Q}$ iCDW order involving only one V orbital, which is shown more schematically in Fig. 5(a), the loop currents close only at the edges of the system. In contrast, the triple-$\mathbf{Q}$ iCDW configuration, consisting of an equal superposition of the three single-$\mathbf{Q}$ order parameters Φ_i^μ features the closed loops shown in Fig. 5(b). The properties of this type of order were previously considered in Refs. [50,51].

B. Interorbital rCDW and iCDW

Interorbital charge orders are constructed by combining fermions from different types of occupied saddle points (M_1^+ and M_4^+) at two different M points. This case is more involved than the intraorbital one, as only symmetric (s) and antisymmetric (a) combinations of the interband bilinears transform as irreps of the little group (see Appendix B). For the rCDW case, we find

$$N_i^s = \sum_{\mathbf{k}\sigma} \langle c^\dagger_{\mathbf{k}+\mathbf{Q}_j\sigma} d_{\mathbf{k}+\mathbf{Q}_l\sigma} + c^\dagger_{\mathbf{k}+\mathbf{Q}_l\sigma} d_{\mathbf{k}+\mathbf{Q}_j\sigma} + \text{H.c.}\rangle, \tag{6}$$

$$N_i^a = \sum_{\mathbf{k}\sigma} \langle c^\dagger_{\mathbf{k}+\mathbf{Q}_j\sigma} d_{\mathbf{k}+\mathbf{Q}_l\sigma} - c^\dagger_{\mathbf{k}+\mathbf{Q}_l\sigma} d_{\mathbf{k}+\mathbf{Q}_j\sigma} + \text{H.c.}\rangle, \tag{7}$$

which transform as the M_3^+ and M_4^+ irreps, respectively. As mentioned above, experimental evidence, as well as DFT calculations, point to the rCDW order transforming as M_1^+ as the one realized experimentally [39,40,44,48,53,60]. Therefore, we will not discuss the M_3^+ and M_4^+ rCDW orders further.

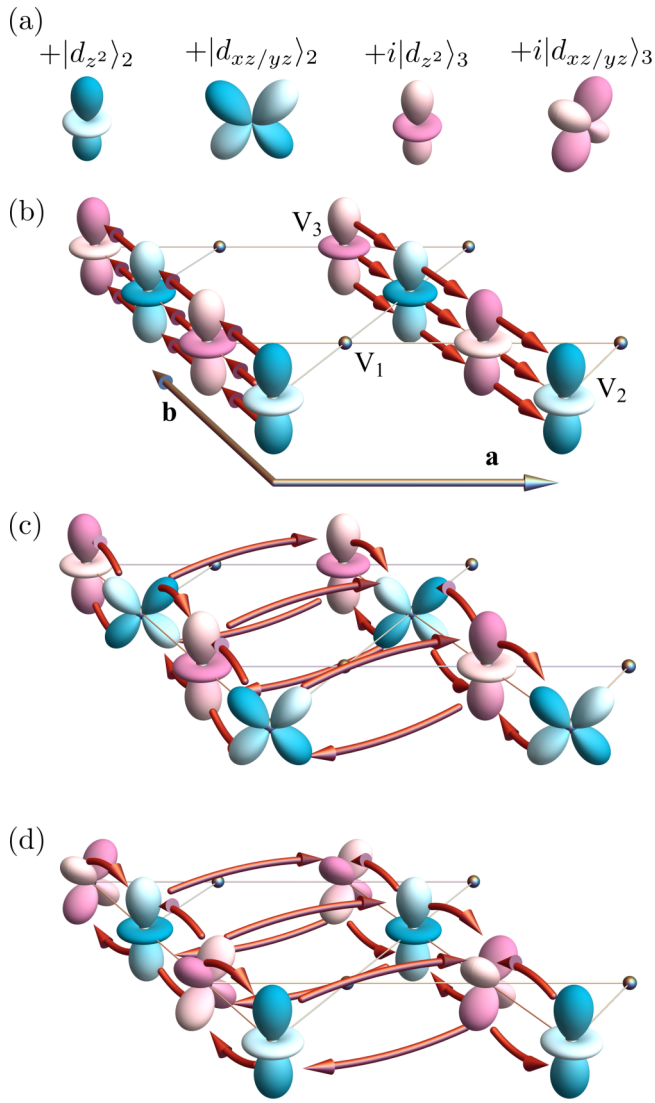

FIG. 4. Schematics of the different constituents of the possible iCDW phases involving the occupied vHs, in terms of currents involving the A_g orbitals (d_{z^2}) and the B_{2g} orbitals (d_{xz}). Panel (a) defines the phase of the orbitals, and [(b)–(d)] refer to iCDW order along M_1, where the Bloch states are centered on the V_2 and V_3 sites. While (b) corresponds to the mM_2^+ intraorbital iCDW phase, the mM_3^+ and mM_4^+ interorbital iCDW phases are the symmetric and antisymmetric combinations of (c) and (d), respectively.

In contrast, the properties of the possible iCDW order are not known from either experiments or first-principles calculations. Similar to the rCDW case, it is necessary to form symmetric and antisymmetric combinations of the fermion bilinears to construct proper iCDW order parameters,

$$\Phi_i^s = i\sum_{\mathbf{k}\sigma}\langle c^\dagger_{\mathbf{k}+\mathbf{Q}_j\sigma} d_{\mathbf{k}+\mathbf{Q}_l\sigma} + c^\dagger_{\mathbf{k}+\mathbf{Q}_l\sigma} d_{\mathbf{k}+\mathbf{Q}_j\sigma} - \text{H.c.}\rangle, \quad (8)$$

$$\Phi_i^a = i\sum_{\mathbf{k}\sigma}\langle c^\dagger_{\mathbf{k}+\mathbf{Q}_j\sigma} d_{\mathbf{k}+\mathbf{Q}_l\sigma} - c^\dagger_{\mathbf{k}+\mathbf{Q}_l\sigma} d_{\mathbf{k}+\mathbf{Q}_j\sigma} - \text{H.c.}\rangle. \quad (9)$$

We find that, while Φ_i^s transforms as the mM_3^+ irrep of $P6/mmm$, Φ_i^a transforms as mM_4^+. In terms of the symmetry operations of the little group D_{2h}, Φ_i^s breaks the twofold rotational symmetry with respect to the out-of-plane axis, whereas Φ_i^a breaks also the twofold rotational symmetry with respect to the in-plane axis [see Table I and Fig. 1(a)].

The loop current patterns generated by these types of iCDW order can be obtained by combining the two interorbital current patterns shown in Figs. 4(c) and 4(d) according to Eqs. (8) and (9). The resulting single-**Q** symmetric combination (mM_3^+), corresponding to Φ_1^s, is shown schematically in Figs. 5(c) and 5(e), and connects the V_2 and V_3 sites on opposite sides of the hexagon. Notably, the current density associated with this iCDW order vanishes on the kagome layer and thus does not lead to a current on the V atoms. However, net currents are induced both above and below the kagome layer, which must necessarily involve the apical Sb atoms. Note that the simultaneous presence of currents above and below the plane implies that charge is conserved for these configurations as well. The fact that there is no current on the V atoms despite the iCDW order parameter being constructed from operators of V atomic orbitals can be understood from the structure of the orbitals in question. Indeed, the mM_3^+ order parameter mixes orbitals with and without a node on the kagome plane itself, as shown in Figs. 4(c) and 4(d). As a consequence, such an iCDW phase is only possible in a multiorbital model. The triple-**Q** configuration of the mM_3^+ iCDW is shown in Figs. 5(d) and 5(f), and consists of counter-circulating loops above and below the plane, which coincide in a single hexagon. In contrast to the triple-**Q** mM_2^+ iCDW configuration, it does not give rise to a dipole moment. We will see this manifested in Sec. V as well.

Finally, the single-**Q** and triple-**Q** configurations associated with the antisymmetric (mM_4^+) iCDW order, described by Φ_1^a, are depicted in Figs. 5(g)–5(j). Like the mM_3^+ case, these configurations feature no net currents in the kagome layer itself. Moreover, the triple-**Q** case also consists of counter-circulating loops above and below the plane that, once again, results in no uniform dipole moment.

In Table II, we summarize our results for the symmetry properties of the rCDW and iCDW order parameters formed out of fermions from the two vHs below the Fermi level.

IV. MIXED REAL AND IMAGINARY CHARGE-ORDER CONFIGURATIONS: OCCUPIED VHS

Experimentally, the condensation of a CDW order at T_{CDW} has been attributed to the softness of a specific M_1^+ phonon mode [39,40,44,48,53]. Since iCDW states transforming as M_1^+ (or mM_1^+) do not appear, this soft phonon has been interpreted as signaling the onset of an rCDW phase, corresponding to charge bond order. However, this does not explain the observations of time-reversal symmetry breaking below T_{CDW} [21,27,63,81]. Instead, these observations could be explained by an iCDW. To reconcile these two scenarios, it has been pointed out that a multi-**Q** iCDW necessarily triggers an rCDW due to the existence of trilinear terms in the free-energy expansion of the coupled iCDW-rCDW order parameters [50,51]. As a result, an iCDW instability may be enough to explain the observations of both a soft M_1^+ phonon mode and the spontaneous breaking of time-reversal symmetry below T_{CDW}.

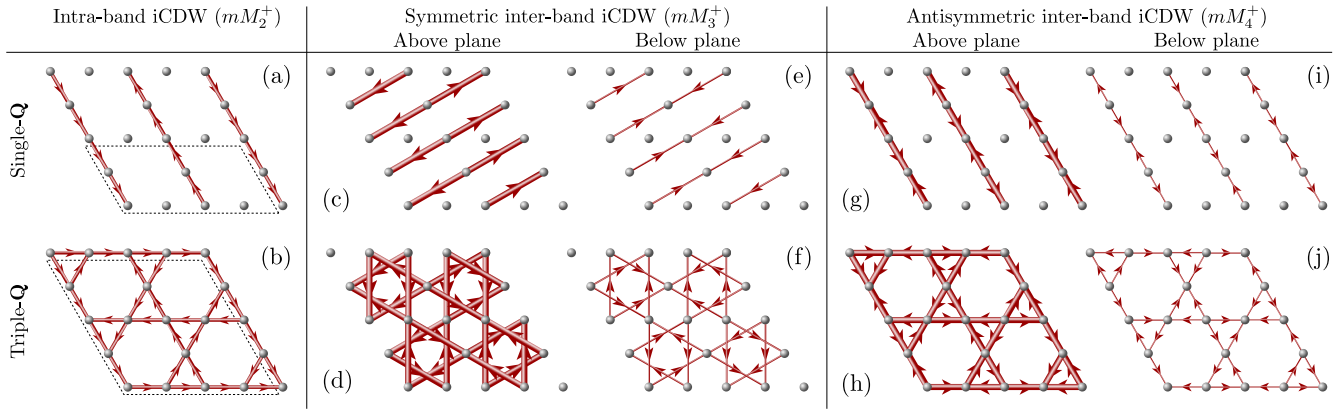

FIG. 5. Illustration of the single-**Q** (upper panels) and triple-**Q** (lower panels) configurations associated with each of the three distinct types of iCDW order arising from the occupied vHs. The latter are labeled here by the M-point irrep of the $P6/mmm$ space group according to which they transform. The intraorbital iCDW order, transforming as mM_2^+ [(a),(b)], gives rise to currents in the kagome plane. The two types of interorbital iCDW order, mM_3^+ [(c)–(f)] and mM_4^+ [(g)-(j)], promote counter-propagating currents above and below the kagome planes, as discussed in the main text. Note that for the mM_3^+ and mM_4^+ cases, the configurations above and below the plane coexist. The dashed lines in (a) and (b) denote the 2×1 and 2×2 unit cells of the single-**Q** and triple-**Q** configurations. The thicker (thinner) arrows in [(c)–(j)] refer to currents above (below) the plane. Note that, due to the coexistence of the above- and below-plane configurations in [(c)–(j)], all states depicted here are charge-conserving.

Reference [50] explored the case in which a triple-**Q** iCDW induces a triple-**Q** rCDW—a mixed iCDW-rCDW configuration that we dub 3**Q**-3**Q**. As we show in this section, there is another viable mixed configuration in which a double-**Q** iCDW and a single-**Q** rCDW coexist—which we denote 2**Q**-1**Q**. To study the possible mixed iCDW-rCDW configurations, we construct the free energy of the high-symmetry phase by finding all possible polynomials of N_i and Φ_i that remain invariant under the symmetry operations of the space group, as well as time reversal symmetry [82,83]. While we restrict N_i to be a M_1^+ rCDW (i.e., an intraorbital rCDW), we allow Φ_i to be any of three possible iCDW states constructed from the occupied vHs (see Table II), i.e., intraorbital (mM_2^+), symmetric interorbital (mM_3^+), and antisymmetric interorbital (mM_4^+). It turns out that, in all cases, the Landau free-energy expansion acquires the same form

$$\mathcal{F}_{\rm CDW} = \mathcal{F}_{\rm r} + \mathcal{F}_{\rm i} + \mathcal{F}_{\rm i-r}, \tag{10}$$

with the rCDW and iCDW free energies

$$\mathcal{F}_{\rm r} = \frac{a_{\rm r}}{2}N^2 + \frac{\gamma_{\rm r}}{3}N_1N_2N_3 + \frac{u_{\rm r}}{4}N^4 + \frac{\lambda_{\rm r}}{4}\left(N_1^2N_2^2 + N_1^2N_3^2 + N_2^2N_3^2\right), \tag{11}$$

$$\mathcal{F}_{\rm i} = \frac{a_{\rm i}}{2}\Phi^2 + \frac{u_{\rm i}}{4}\Phi^4 + \frac{\lambda_{\rm i}}{4}\left(\Phi_1^2\Phi_2^2 + \Phi_1^2\Phi_3^2 + \Phi_2^2\Phi_3^2\right), \tag{12}$$

and the coupling between them given by

$$\begin{aligned}\mathcal{F}_{\rm i-r} =& \frac{\gamma_{\rm ir}}{3}(N_1\Phi_2\Phi_3 + \Phi_1N_2\Phi_3 + \Phi_1\Phi_2N_3) \\ &+ \frac{\kappa_{\rm ir}}{4}\left(N_1N_2\Phi_1\Phi_2 + N_1N_3\Phi_1\Phi_3 + N_2N_3\Phi_2\Phi_3\right) \\ &+ \frac{\lambda_{\rm ir}^{(1)}}{4}\left(N_1^2\Phi_1^2 + N_2^2\Phi_2^2 + N_3^2\Phi_3^2\right) \\ &+ \frac{\lambda_{\rm ir}^{(2)}}{4}N^2\Phi^2.\end{aligned} \tag{13}$$

In these expressions, $N^2 \equiv \sum_i N_i^2$ and $\Phi^2 \equiv \sum_i \Phi_i^2$. The quadratic Landau coefficients are defined in the standard way, $a_\mu = a_{\mu,0}(T - T_\mu)$, with $\mu = {\rm r}, {\rm i}$, the coefficient $a_{\mu,0} > 0$ and T_μ denote the bare transition temperatures. The Landau coefficients u_μ refer to quartic terms; γ_μ, to trilinear terms; λ_μ, to biquadratic terms; and κ_μ, to quadrilinear terms. Note that, while the little group irreps have uniquely defined matrices, the space group irreps are arbitrary up to minus signs in certain off diagonal elements, which do not affect their characters. Similarly, shifting the origin by a unit cell changes the signs of certain components of the order parameters. As a result, the sign of the trilinear term is arbitrary, and is valid only for a fixed origin choice.

The fact that the bare iCDW and rCDW transition temperatures are different, $T_{\rm r} \neq T_{\rm i}$, is a consequence of the two order parameters transforming as different irreps. Nevertheless, the renormalization-group calculation of Ref. [50] found that for certain regimes of the interaction parameters, the two transition temperatures can be comparable. Even if this is not the case, a sufficiently strong trilinear coefficient $\gamma_{\rm ir}$ will generally cause the two transitions to happen simultaneously and in a first-order fashion, regardless of the sign of $\gamma_{\rm ir}$.

The free energy in Eq. (10) allows for various types of mixed phases. To gain insight into the typical global minima of this free energy, we note that it has the exact same functional form as the free energy for the coupled in-plane and out-of-plane rCDW orders studied by us in Ref. [54]. In that case, it was shown that much of the phase diagram is dominated by two phases in particular, which in our situation translate to a 3**Q**-3**Q** phase, where all three N_i and all three Φ_i are nonzero, and to a 2**Q**-1**Q** phase, where only Φ_i, Φ_j, and N_l are nonzero, with (i, j, l) denoting a permutation of (1,2,3). Indeed, it is clear that these two mixed configurations are those that minimize the energy of the trilinear term with coefficient $\gamma_{\rm ir}$. Whether the 3**Q**-3**Q** or the 2**Q**-1**Q** phase is realized depends on the quadrilinear and biquadratic coefficients, as discussed in Ref. [54].

TABLE II. Possible rCDW and iCDW order parameters constructed from the $c^\dagger_{\mathbf{k}\sigma}$ and $d^\dagger_{\mathbf{k}\sigma}$ fermionic operators. The latter refer to energy eigenstates of the M_1^+ and M_4^+ occupied saddle points, respectively. M_i^+ are irreps of the little group of the M point of the space group $P6/mmm$. As explained in the text, the interorbital CDW orders are obtained as symmetric and antisymmetric combinations of the interorbital fermionic bilinears. In the equations below, (i, j, l) is a permutation of (1,2,3).

Order	Order parameter(s)	Irrep
rCDW	$N_i^c = \sum_{\mathbf{k}\sigma}\langle c^\dagger_{\mathbf{k}+\mathbf{Q}_j\sigma} c_{\mathbf{k}+\mathbf{Q}_l\sigma} + \text{H.c.}\rangle$	M_1^+
	$N_i^d = \sum_{\mathbf{k}\sigma}\langle d^\dagger_{\mathbf{k}+\mathbf{Q}_j\sigma} d_{\mathbf{k}+\mathbf{Q}_l\sigma} + \text{H.c.}\rangle$	
	$N_i^s = \sum_{\mathbf{k}\sigma}\langle c^\dagger_{\mathbf{k}+\mathbf{Q}_j\sigma} d_{\mathbf{k}+\mathbf{Q}_l\sigma} + c^\dagger_{\mathbf{k}+\mathbf{Q}_l\sigma} d_{\mathbf{k}+\mathbf{Q}_j\sigma} + \text{H.c.}\rangle$	M_3^+
	$N_i^a = \sum_{\mathbf{k}\sigma}\langle c^\dagger_{\mathbf{k}+\mathbf{Q}_j\sigma} d_{\mathbf{k}+\mathbf{Q}_l\sigma} - c^\dagger_{\mathbf{k}+\mathbf{Q}_l\sigma} d_{\mathbf{k}+\mathbf{Q}_j\sigma} + \text{H.c.}\rangle$	M_4^+
iCDW	$\Phi_i^c = i\sum_{\mathbf{k}\sigma}\langle c^\dagger_{\mathbf{k}+\mathbf{Q}_j\sigma} c_{\mathbf{k}+\mathbf{Q}_l\sigma} - \text{H.c.}\rangle$	mM_2^+
	$\Phi_i^d = i\sum_{\mathbf{k}\sigma}\langle d^\dagger_{\mathbf{k}+\mathbf{Q}_j\sigma} d_{\mathbf{k}+\mathbf{Q}_l\sigma} - \text{H.c.}\rangle$	
	$\Phi_i^s = i\sum_{\mathbf{k}\sigma}\langle c^\dagger_{\mathbf{k}+\mathbf{Q}_j\sigma} d_{\mathbf{k}+\mathbf{Q}_l\sigma} + c^\dagger_{\mathbf{k}+\mathbf{Q}_l\sigma} d_{\mathbf{k}+\mathbf{Q}_j\sigma} - \text{H.c.}\rangle$	mM_3^+
	$\Phi_i^a = i\sum_{\mathbf{k}\sigma}\langle c^\dagger_{\mathbf{k}+\mathbf{Q}_j\sigma} d_{\mathbf{k}+\mathbf{Q}_l\sigma} - c^\dagger_{\mathbf{k}+\mathbf{Q}_l\sigma} d_{\mathbf{k}+\mathbf{Q}_j\sigma} - \text{H.c.}\rangle$	mM_4^+

Of course, it is also possible to realize nonmixed phases, such as a pure triple-**Q** rCDW phase or a pure single-**Q** iCDW phase. The latter is the only case in which iCDW order does not trigger rCDW order, as also discussed in Ref. [50]. Because these nonmixed phases cannot explain the experimental observations of time-reversal symmetry breaking and a 2×2 increase of the unit cell, we will focus on the mixed iCDW-rCDW phases hereafter.

Figure 6 illustrates both types of mixed rCDW-iCDW phases, 3**Q**-3**Q** and 2**Q**-1**Q**, for the particular case of an intraorbital mM_2^+ iCDW order parameter. As explained above, we are only considering the intraorbital rCDW order, as it transforms as M_1^+. As expected, the kagome lattice displays not only bond distortions but also loop currents. We emphasize that a pure double-**Q** iCDW phase or a pure triple-**Q** iCDW phase are not minima of the free energy, as they can only arise in conjunction with rCDW order. Moreover, for the 3**Q**-3**Q** phase, while the sign of the product $\Phi_1\Phi_2\Phi_3$ does not change the loop-currents configuration [50], the sign of $N_1N_2N_3$ distinguishes between a star-of-David and a trihexagonal bond-order configuration [54].

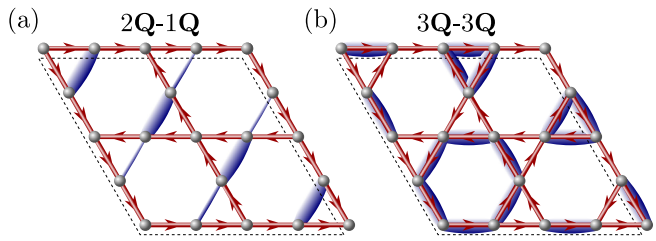

FIG. 6. Illustration of the two mixed iCDW-rCDW phases that can minimize the coupled free energy, Eq. (10). For concreteness, we show the case of intraorbital iCDW order (i.e., mM_2^+) made out of the states from the same vHs. The rCDW order is also intraorbital (i.e., M_1^+). (a) The 2**Q**-1**Q** phase consists of a double-**Q** iCDW phase combined with a single-**Q** rCDW, such that the three wave vectors are a permutation of $(\mathbf{Q}_1, \mathbf{Q}_2, \mathbf{Q}_3)$. Blue bonds denote the bond distortions promoted by the rCDW order, whereas the red arrows denote the currents generated by the iCDW order. (b) The 3**Q**-3**Q** phase consists of a triple-**Q** iCDW coexisting with a triple-**Q** rCDW phase.

V. EXPERIMENTAL SIGNATURES OF THE MIXED CDW STATES: OCCUPIED VHS

By focusing on the low-energy electronic states near the two vHs below the Fermi level at the M point, we found three possible types of iCDW states, illustrated in Fig. 5: intraorbital (mM_2^+), symmetric interorbital (mM_3^+), and antisymmetric interorbital (mM_4^+). When coupled to the intraorbital rCDW order parameter (M_1^+), they in turn give rise to two different types of mixed iCDW-rCDW states, denoted 3**Q**-3**Q** and 2**Q**-1**Q**, illustrated in Fig. 6 in the case of intraorbital iCDW order. There are therefore six different candidate CDW states formed out of the occupied vHs that could explain the experimental observations of a 2×2 unit cell increase and time-reversal symmetry breaking below T_{CDW}. In this section, we discuss the experimental signatures of these six states, focusing on the magnetic and structural properties that can be probed experimentally to unambiguously distinguish between them. A summary of the results of this section and of Sec. VI is contained in Table III for convenience.

A. Finite-momentum magnetism: Spin-density wave

In the presence of spin-orbit coupling, the iCDW orders must necessarily induce spin-density wave (SDW) orders [76]. Indeed, an iCDW corresponds to an imaginary hopping between two sites on the lattice. This leads to ordering of the electrons' orbital angular momentum, which in turn results in ordering of the spin angular momentum in the presence of spin-orbit coupling.

In terms of symmetry, we can define other fermionic bilinears built out of the Bloch states of the saddle points that transform as the same irreps as the iCDW order parameters. For instance, consider the intraorbital SDW order parameter with wave vector $\mathbf{Q}_1$,

$$\vec{\Delta}_1 = \sum_{\mathbf{k}\sigma\sigma'}\langle c^\dagger_{\mathbf{k}+\mathbf{Q}_2,\sigma}\vec{\tau}_{\sigma\sigma'} c_{\mathbf{k}+\mathbf{Q}_3,\sigma'} + \text{H.c.}\rangle, \tag{14}$$

where τ^i denotes a Pauli matrix in spin-space. Using the local coordinate system of V_1 to label the spin directions, it turns out that Δ_1^z transforms as mM_2^+, Δ_1^x transforms as mM_3^+, and Δ_1^y, as mM_4^+. However, the directions of the in-plane spins for the mM_3^+ and mM_4^+ order parameters are different for different

TABLE III. Summary of the different types of mixed iCDW-rCDW configurations found in this work, arising from the low-energy electronic states associated with the two occupied vHs (p_--type) and the two unoccupied vHs (p_+-type and m-type) shown in Fig. 1(c). Note that, in rows 4 and 5, p_- refers only to the occupied vHs closest to the Fermi level. In all cases, the rCDW is described by an M_1^+ order parameter, whereas the iCDW order parameter $\mathbf{\Phi}$ is given by the second column of the table. There are two different kinds of mixed state, 3**Q**-3**Q** and 2**Q**-1**Q**. The first displays different types of subsidiary uniform magnetic order, whose order parameter μ scales as Φ^3, whereas the latter displays only an orthorhombic distortion η that scales quadratically with Φ. For each subsidiary order we include both the space group irreps (using the convention of Ref. [84]) and point group irreps (using the convention of Ref. [85]; in the first seven rows, the irreps are odd under time-reversal whereas in the last two rows, it is even). The fourth column shows which combination of external fields couples to the subsidiary order parameter μ or $\boldsymbol{\eta}$. Here, **B** is the magnetic field, **E** is the electric field, and $\boldsymbol{\varepsilon}_\parallel$ is the in-plane strain field given by Eq. (16). The last column shows the name and number of the magnetic space groups (M.S.G.) of each mixed state in the Belov-Neronova-Smirnova notation. Primed operations refer to point symmetry operations followed by time reversal. For example, $6'$ denotes a 60° rotation followed by time-reversal, and m' denotes a mirror reflection followed by time reversal.

Mixed iCDW-rCDW	iCDW type	Subsidiary order	External field coupling	M.S.G.
	Any intraorbital	Ferromagnetic	B_z	$P6/mm'm'$
	(mM_2^+)	$(m\Gamma_2^+,\ A_{2g})$		(#191.240)
	p_--p_- symm. interorbital	Magnetic octupolar	$(\mathbf{B}_\parallel \times \boldsymbol{\varepsilon}_\parallel)\cdot\hat{\mathbf{z}}$	$P6'/m'mm'$
	(mM_3^+)	$(m\Gamma_3^+,\ B_{2g})$		(#191.239)
	p_--p_- antisymm. interorbital	Magnetic octupolar	$\mathbf{B}_\parallel \cdot \boldsymbol{\varepsilon}_\parallel$	$P6'/m'm'm$
	(mM_4^+)	$(m\Gamma_4^+,\ B_{1g})$		(#191.238)
3**Q**-3**Q**	p_--m symm. interorbital	Magnetic monopolar	$E_zB_z,\ \mathbf{E}_\parallel \cdot \mathbf{B}_\parallel$	$P6'/m'm'm'$
($\mu \sim \Phi^3$)	(mM_1^-)	$(m\Gamma_1^-,\ A_{1u})$		(#191.241)
	p_--m antisymm. interorbital	Magnetic toroidal dipolar	$(\mathbf{E}\times\mathbf{B})\cdot\hat{\mathbf{z}}$	$P6/m'mm$
	(mM_2^-)	$(m\Gamma_2^-,\ A_{2u})$		(#191.235)
	p_+-m symm. interorbital	Magnetic toroidal octupolar	$E_z(\mathbf{B}_\parallel \cdot \boldsymbol{\varepsilon}_\parallel)$	$P6'/mm'm$
	(mM_3^-)	$(m\Gamma_3^-,\ B_{2u})$		(#191.236)
	p_+-m antisymm. interorbital	Magnetic toroidal octupolar	$\mathbf{E}\cdot(\mathbf{B}_\parallel \times \boldsymbol{\varepsilon}_\parallel)$	$P6'/mmm'$
	(mM_4^-)	$(m\Gamma_4^-,\ B_{1u})$		(#191.237)
2**Q**-1**Q**	mM_2^+, mM_3^-, mM_4^-	Orthorhombic distortion	$\boldsymbol{\varepsilon}_\parallel$	C_ammm
($\eta \sim \Phi^2$)		$(m\Gamma_5^+,\ E_{2g})$		(#65.489)
	$mM_3^+, mM_4^+, mM_1^-, mM_2^-$	Orthorhombic distortion	$\boldsymbol{\varepsilon}_\parallel$	C_amma
		$(m\Gamma_5^+,\ E_{2g})$		(#67.509)

wave vectors. As a result, labeling these order parameters with a Cartesian direction could be misleading. Instead, we note that the mM_3^+ order parameter gives rise to a spin stripe with spins normal to the wave vector, whereas for mM_4^+ the spins are parallel to the wave vector. As a result, we refer to the mM_3^+ and mM_4^+ SDW orders as $\Delta_i^\perp$ and $\Delta_i^\parallel$ respectively, instead of Δ_i^x and Δ_i^y.

Since there are SDW order parameters that transform as the same irrep as the iCDW order parameters, the condensation of the iCDW order parameter Φ_1 leads to the condensation of an intraorbital SDW at the same wave vector, since it is bilinearly coupled in the free energy to one of the components of $\vec{\Delta}$. In particular, the magnetic moments in the SDW phase are polarized along different axes depending on the nature of the iCDW state: z axis, for intraorbital iCDW; the axis normal to the wave vector, for symmetric interorbital iCDW; and the axis parallel to the wave vector, for antisymmetric interorbital iCDW.

This result provides another route to probe the existence of an iCDW, as neutron scattering experiments could in principle directly assess the existence of SDW order from the magnetic Bragg peaks that it creates. Of course, the feasibility of such a measurement will depend on the size of the SDW magnetic moment. Interestingly, polarized neutron scattering could further distinguish between the three different types of iCDW by determining the direction of the moments. One important caveat related to this last point is that interorbital SDW can also be induced, but with a moment direction that is generally different from that of the order parameter in Eq. (14).

Figure 7 illustrates the magnetic patterns of the SDW phases induced by single-**Q** (a), double-**Q** (b), and triple-**Q** (c) intraband iCDW order. Rather than determining these magnetic configurations indirectly from the loop-current patterns, here we directly derive them from the symmetry properties of the relevant irrep—which in this case is mM_2^+. As expected, a single-**Q** iCDW generates a stripe SDW with the moments oriented out-of-plane. Interestingly, in both the double- and triple-**Q** phases, the superposition of the different stripe SDWs results in peaks of the magnetization density at the Sb sites, rather than the V sites.

B. Uniform magnetism: Ferromagnetism and magnetic octupolar order

In addition to the SDW orders that accompany the onset of iCDW orders, different types of subsidiary *uniform* magnetic order also appear in the mixed iCDW-rCDW phases. They are described by the scalar order parameter

$$\mu = \Phi_1\Phi_2\Phi_3 \propto \mathbf{N}\cdot\mathbf{\Phi}, \tag{15}$$

which is clearly odd under time reversal and has zero wave vector. Note that μ is only nonzero in the 3**Q**-3**Q** mixed phase, and the 2**Q**-1**Q** phase does not display subsidiary uniform magnetic order.

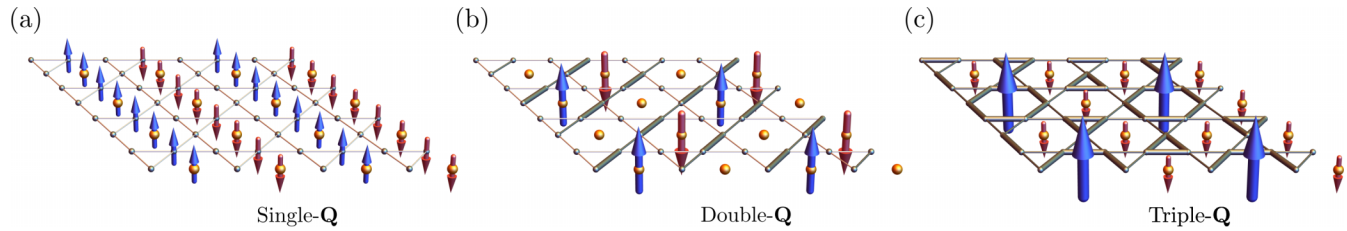

FIG. 7. Illustrations of the spin-density wave patterns induced by intraorbital iCDW in the case of single-**Q** [panel(a)], double-**Q** [panel(b)], and triple-**Q** [panel(c)] order. Note that the spin-density wave has peaks at the Sb atoms, rather than at the V atoms. In panels (b) and (c), corresponding to the 2**Q**-1**Q** and 3**Q**-3**Q** states, respectively, rCDW order must accompany the iCDW one. The bond-distortion patterns corresponding to these rCDW orders are illustrated as well. In the 3**Q**-3**Q** case, the local environment experienced by the sites with spin-up is different from that experienced by the sites with spin-down, resulting in a net magnetic moment.

Importantly, the transformation properties of μ, and thus the nature of the uniform magnetic order, depend crucially on the type of iCDW order. For intraorbital iCDW order (mM_2^+), μ transforms as the time-reversal-odd A_{2g} irrep of the D_{6h} point group (or, equivalently, $m\Gamma_2^+$ of $P6/mmm$ using the notation of INVARIANTS, which follows the Cracknell-Davies-Miller-Love tables [85,86]). Therefore, μ corresponds to ferromagnetic order with moments pointing out-of-plane, as illustrated in Fig. 8(a). This is in agreement with the SDW pattern shown in Fig. 7(c): in a single unit cell there are smaller moments at three Sb sites pointing in one direction and a bigger moment at another Sb site pointing in the opposite direction. Because the local environments experienced by the two types of Sb sites are inequivalent due to the accompanying bond-distortion pattern, the four moments do not cancel, and a net dipolar magnetic moment is generated. Alternatively, one can conclude that a net magnetic moment must be present because the application of time-reversal symmetry cannot be undone by a translation. We note that Ref. [50] previously pointed out that a triple-**Q** iCDW order induces an out-of-plane magnetization. Indeed, the magnetic space group of the 3**Q**-3**Q** configuration with intraband iCDW order, shown in the last column of Table III, allows a nonzero out-of-plane magnetic dipole moment.

From the definition of μ, we conclude that the induced magnetization scales as $|\mathbf{\Phi}|^3$, where $|\mathbf{\Phi}|$ is the magnitude of the iCDW order parameter. Thus, because the induced SDW Δ^z scales linearly with $|\mathbf{\Phi}|$, there is a well-defined relationship between the uniform magnetization and the finite-momentum magnetization, $\mu \sim (\Delta^z)^3$. This result provides yet another route to probe iCDW order in AV_3Sb_5 through a coupling to the SDW order.

In the case of interorbital iCDW orders, a finite μ implies different types of uniform magnetic orders, as it transforms as the time-reversal odd B_{2g} and B_{1g} irreps of D_{6h} for the symmetric (mM_3^+) and antisymmetric (mM_4^+) types of iCDW order, respectively. In terms of the irreps of the space group $P6/mmm$, they correspond to $m\Gamma_3^+$ and $m\Gamma_4^+$, respectively. Physically, an order parameter with these transformation properties results in *magnetic octupolar order* [87].

The real-space configuration of magnetic moments associated with these two types of magnetic octupolar order are shown in Figs. 8(b) and 8(c), which we dub transverse [B_{2g}, panel(b)] and longitudinal [B_{1g}, panel (c)] ferro-octupolar orders. In both cases, the magnetic moments point in-plane, but are subjected to different spatial modulations. Neither configuration results in a net magnetic moment, in agreement with the fact that, for the triple-**Q** interband iCDW orders, the loop currents above and below the kagome plane cancel each other, as shown in Fig. 5.

The most straightforward way to probe these subsidiary magnetic octupolar orders is to assess their magnetostriction properties. We start by constructing the following vectors from the in-plane components of the magnetic field and of the strain tensor

$$\mathbf{B}_\parallel = \begin{pmatrix} B_x \\ B_y \end{pmatrix}, \quad \boldsymbol{\varepsilon}_\parallel = \begin{pmatrix} \varepsilon_{x^2-y^2} \\ -\varepsilon_{xy} \end{pmatrix}. \tag{16}$$

Here, $\varepsilon_{ij} \equiv (\partial_i u_j + \partial_j u_i)/2$, where $\mathbf{u}$ denotes the lattice displacement vector. In order to be consistent with the irrep

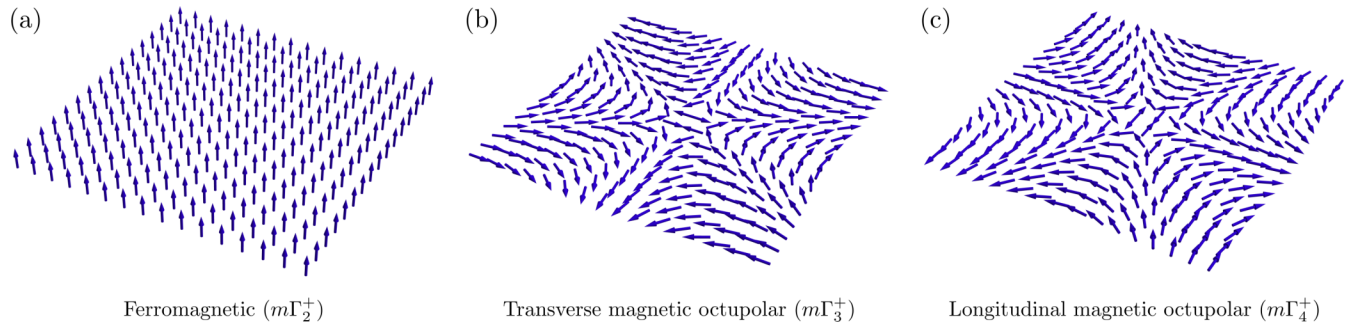

FIG. 8. Illustrations of different types of uniform magnetic order: (a) ferromagnetism; (b) transverse magnetic octupolar order; and (c) longitudinal magnetic octupolar order. These subsidiary orders appear in the 3**Q**-3**Q** states with intraband, symmetric interband, and antisymmetric interband iCDW orders generated from the occupied vHs, respectively.

matrices of Ref. [83], we choose a global coordinate axis with $\hat{\mathbf{y}}$ parallel to the crystallographic a axis (the [100] direction). Using the fact that $\mathbf{B}_\parallel$ transforms as the $m\Gamma_6^+$ irrep, whereas $\boldsymbol{\varepsilon}_\parallel$ transforms as Γ_5^+, we derive the following magnetostriction free-energy term in the 3**Q**-3**Q** state with symmetric interorbital iCDW order:

$$\mathcal{F}_{\mathrm{mag-str}}^{(mM_3^+)} \sim \mu(\mathbf{B}_\parallel \times \boldsymbol{\varepsilon}_\parallel)\cdot\hat{\mathbf{z}}, \tag{17}$$

where μ is the magnetic octupolar moment defined in Eq. (15). Conversely, for the 3**Q**-3**Q** state with antisymmetric interorbital iCDW order, we find

$$\mathcal{F}_{\mathrm{mag-str}}^{(mM_4^+)} \sim \mu(\mathbf{B}_\parallel \cdot \boldsymbol{\varepsilon}_\parallel). \tag{18}$$

The first of these equations, Eq. (17), implies that, in the 3**Q**-3**Q** state with symmetric interorbital iCDW order, application of an in-plane magnetic field generates strain in the "transverse" direction (in the abstract subspace of two dimensional irreps). For example, a magnetic field applied along the y axis (which is the crystallographic a axis) will generate the strain component $\epsilon_{x^2-y^2}$. In contrast, in the case of antisymmetric interorbital iCDW order, the strain generated by an in-plane magnetic field is "longitudinal"—e.g., a finite B_y induces ϵ_{xy}. Of course, the reverse is also true: shear strain ϵ_{xy} induces magnetic moments along the y axis in the latter case and along the x axis in the former. These unique magnetostriction properties could be used to experimentally probe the character of the 3**Q**-3**Q** phases. A summary of these results is contained in Table III.

C. Lattice distortion: Threefold rotational symmetry breaking

While the 3**Q**-3**Q** states display uniform magnetic order, the 2**Q**-1**Q** states are accompanied by a uniform lattice distortion that breaks the threefold rotational symmetry of the kagome lattice. This is apparent in Fig. 6(a), as the loop-current and bond-distortion patterns are not invariant under 120° rotation. Formally, we can construct an order parameter that is quadratic in the iCDW order parameters and transforms as the same Γ_5^+ irrep as the in-plane strain $\boldsymbol{\varepsilon}_\parallel$ defined in Eq. (16),

$$\boldsymbol{\eta}_1 = \begin{pmatrix} \Phi_1^2 + \Phi_3^2 - 2\Phi_2^2 \\ \sqrt{3}\left(\Phi_3^2 - \Phi_1^2\right) \end{pmatrix}. \tag{19}$$

Clearly, $\boldsymbol{\eta}_1$ is only nonzero in the 2**Q**-1**Q** phase, leading to an orthorhombic distortion of the lattice. Similarly, we can define an order parameter that also transforms as Γ_5^+ and that depends explicitly on the rCDW order parameter **N**,

$$\boldsymbol{\eta}_2 = \begin{pmatrix} N_1\Phi_2\Phi_3 + \Phi_1\Phi_2N_3 - 2\Phi_1N_2\Phi_3 \\ \sqrt{3}(\Phi_1\Phi_2N_3 - N_1\Phi_2\Phi_3) \end{pmatrix}. \tag{20}$$

Note that, in contrast to $\boldsymbol{\eta}_1$, $\boldsymbol{\eta}_2$ is quartic in $\boldsymbol{\Phi}$.

Recent experiments have reported the breaking of the threefold rotational symmetry of the kagome lattice inside the CDW phase of the AV_3Sb_5 compounds [38,46,47,62,63,74]. In contrast to time-reversal symmetry breaking, however, the rotational symmetry seems to be broken only well below T_{CDW}. Therefore, this type of order does not onset before the CDW and breaks translational symmetry; as such, it should not be classified as a nematic phase.

Previously, the breaking of threefold rotational symmetry was proposed to arise from an admixture between two real CDWs, one with and one without out-of-plane modulation [39,50,54]. Our analysis shows that it could also be explained by an admixture between real and imaginary CDWs in the 2**Q**-1**Q** state, without the need to invoke an out-of-plane component of the wave vector. In this respect, it is tempting to attribute the experimental observations to a transition from the 3**Q**-3**Q** phase to the 2**Q**-1**Q** phase. However, in several of these experiments, the threefold rotational symmetry breaking was observed in the presence of an in-plane magnetic field, which presumably aligns the different orthorhombic domains. As we showed in the previous subsection, $\mathbf{B}_\parallel$ induces a finite orthorhombic distortion $\boldsymbol{\varepsilon}_\parallel$ in the 3**Q**-3**Q** phase with interorbital iCDW order. Therefore, to shed light on this issue, it is important that future experiments clarify the relationship between the in-plane field and the threefold rotational symmetry breaking.

D. Impact of out-of-plane modulation

Our analysis so far has focused solely on iCDW and rCDW orders with in-plane wave vectors $\mathbf{Q}_i$ coinciding with the M_i points of the BZ. X-ray experiments on AV_3Sb_5, however, reveal that the charge-order wave vector can also have a finite commensurate z component, resulting in a $2\times2\times2$ or $2\times2\times4$ unit cell in the ordered state [41,44]. The precise c axis modulation depends not only on the alkali-metal atom A, but also on temperature and pressure [31,61,88].

It is straightforward to extend our analysis to the case of an ordering wave vector along the $\mathrm{M}-\mathrm{L}$ line of the BZ, which we label by its z axis component Q^z. Based on the experimental results mentioned above, we restrict our analysis to two different possible out-of-plane modulations for the iCDW order parameter, $Q^z_{\mathrm{iCDW}} = 1/2$ and $Q^z_{\mathrm{iCDW}} = 1/4$ (in reciprocal lattice vector units). As we saw in Sec. IV, the intrinsic coupling between the iCDW and rCDW order parameters arises from the trilinear term in the free energy of Eq. (13). In order for that term to be preserved, it must follow that

$$Q^z_{\mathrm{rCDW}} = 2\,Q^z_{\mathrm{iCDW}}, \tag{21}$$

i.e., the rCDW modulation must be equal to half of the iCDW modulation. By symmetry, it also follows that the induced SDW has the same modulation as the iCDW, $Q^z_{\mathrm{SDW}} = Q^z_{\mathrm{iCDW}}$.

The properties of the subsidiary order parameters μ and $\boldsymbol{\eta}$ can also be determined in a straightforward way. Because μ is cubic in Φ_i, it has the same z component of the wave vector as the iCDW order parameter, $Q^z_\mu = Q^z_{\mathrm{iCDW}}$ (recall that we are restricting our analysis to $Q^z_{\mathrm{iCDW}} = 1/2, 1/4$). Consequently, in the 3**Q**-3**Q** state, the induced magnetic order is uniform in the kagome planes but exhibits the same modulation along the c axis as the iCDW order parameter. This implies that antiferromagnetic order emerges in the case of intraorbital iCDW; for interorbital iCDW, the same antiferromagnetic pattern arises if uniaxial in-plane stress is applied.

As for $\boldsymbol{\eta}$, which is proportional to the square of Φ, its wave vector remains at the Γ point, i.e., $Q^z_{\boldsymbol{\eta}} = 0$. Consequently, the 2**Q**-1**Q** state displays an orthorhombic distortion regardless of the modulation of the iCDW. To arrive at this conclusion,

it is important to note that, unlike the $Q^z_{\rm iCDW} = 0, 1/2$ cases, the iCDW order parameter becomes a *complex-valued* three-component order parameter for $Q^z_{\rm iCDW} = 1/4$, since $\mathbf{Q}_{\rm iCDW} \neq -\mathbf{Q}_{\rm iCDW}$. As a result, $\boldsymbol{\eta}_1$ in Eq. (19) must be rewritten with $\Phi_i^2 \to |\Phi_i|^2$; in contrast, $\boldsymbol{\eta}_2$ in Eq. (20) remains the same.

VI. CANDIDATE CHARGE ORDERS: UNOCCUPIED VAN HOVE SINGULARITIES

We now repeat the analyses of Secs. III, IV, and V for the iCDW phases that arise from the Bloch states associated with the unoccupied vHs of Fig. 1(c). We recall that the unoccupied vHs closest to the Fermi level transforms as the M_3^+ irrep and is of p type, whereas the second unoccupied vHs closest to the Fermi level is of m type and transforms as the M_2^- irrep. Since the steps are the same as in the previous sections, we do not delve into details of the calculation and just present the main results.

A. iCDW phases from the unoccupied vHs only

Mirroring what we did for the two occupied vHs, we first consider the three different types of iCDW order that emerge from combinations of electronic states associated with the two unoccupied vHs. As shown in the insets of Fig. 1(c), the local d_{yz} orbitals contribute to the M_3^+ vHs whereas the local d_{xz} orbitals contribute to the M_2^- vHs. For this reason, we continue using the nomenclature of intraorbital and interorbital iCDW.

Labeling the electronic states near the M_3^+ vHs by the operator $c^\dagger_{\mathbf{k}\sigma}$ and the electronic states near the M_2^- vHs by $d^\dagger_{\mathbf{k}\sigma}$, we obtain the iCDW order parameters as in Table II. While the intraorbital Φ_i^c and Φ_i^d iCDW order parameters still transform as mM_2^+, the interorbital Φ_i^s and Φ_i^a now transform as mM_3^- and mM_4^-, respectively. Remarkably, they couple to the M_1^+ rCDW order parameter N_i in the same way as their counterparts in Table II, i.e., the coupled iCDW-rCDW Landau free energy acquires the same form as Eq. (10). Consequently, there are two viable mixed iCDW-rCDW states, the 3**Q**-3**Q** and the 2**Q**-1**Q** ones.

The 3**Q**-3**Q** mixed configuration displays subsidiary uniform magnetic order described by the cubic order parameter $\mu \sim \Phi^3$ defined in Eq. (15) above. Like the magnetic octupolar orders generated in the case of interband iCDW order involving the occupied vHs, these subsidiary magnetic orders do not have a net magnetic dipole moment. However, they are odd under inversion, as indicated by their transformation properties: $m\Gamma_3^-$ (or time-reversal odd B_{2u}), for the case of the symmetric interorbital iCDW, and $m\Gamma_4^-$ (or time-reversal odd B_{1u}), for the antisymmetric interorbital iCDW. Therefore, they can be identified as two different types of *magnetic toroidal octupolar* order, following the classification of Ref. [87]. Indeed, the key property of an octupolar magnetic toroidal moment is that it changes sign not only under time reversal, but also under spatial inversion. These magnetic toroidal octupolar orders can be probed experimentally by a combination of magnetic field **B**, in-plane uniaxial strain $\boldsymbol{\varepsilon}_\parallel$, and electric field **E**. Using group theory, we find the following free-energy couplings between the external fields and the magnetic toroidal octupolar moment μ, corresponding to magnetoelectrostriction terms,

$$\mathcal{F}^{(mM_3^-)}_{\rm mag-el-str} \sim \mu\, E_z(\mathbf{B}_\parallel \cdot \boldsymbol{\varepsilon}_\parallel), \tag{22}$$

as well as

$$\mathcal{F}^{(mM_4^-)}_{\rm mag-el-str} \sim \mu\, \mathbf{E} \cdot (\mathbf{B}_\parallel \times \boldsymbol{\varepsilon}_\parallel). \tag{23}$$

Therefore, application of in-plane uniaxial strain induces *multiferroic* order characterized by an in-plane magnetic moment (whose direction can be longitudinal or transverse to the strain direction) and an out-of-plane electric polarization.

As for the 2**Q**-1**Q** mixed configuration, its subsidiary uniform order is not magnetic, but orthorhombic, like in the case of interorbital iCDW made out of the occupied vHs. It is described by the same order parameter $\boldsymbol{\eta}$ defined in Eq. (19), which scales as the square of the iCDW order parameter Φ. Table III summarizes the properties of the mixed iCDW-rCDW states generated by the unoccupied vHs, including the magnetic space groups that describe them.

B. iCDW phases from mixed occupied and unoccupied vHs

So far we have considered the two pairs of vHs—occupied and unoccupied—separately. The reasoning is that the energy separation between these pairs, of the order of 200 meV [see Fig. 1(c)], is significant enough that it is likely to prevent instabilities driven by the coupling between states associated with occupied and unoccupied vHs. Nevertheless, it is possible that this energy splitting could be reduced by correlations not captured by DFT, or by different doping schemes. Moreover, even within DFT, upon moving away from the M point along the M − L line, the energy splitting between the pairs of vHs changes as a function of out-of-plane momentum [8].

Therefore, and for the sake of completeness, we briefly discuss the properties of the possible iCDW order parameters obtained by combining states from vHs above and below the Fermi level. The only combinations that give iCDW orders not already discussed above are the symmetric and antisymmetric interorbital iCDW order parameters made out of states from the m-type vHs and from the p_--type vHs that is closest to the Fermi level. Specifically, the corresponding order parameters Φ_i^s and Φ_i^a, as defined in Table II, transform as the irreps mM_1^- and mM_2^-. The corresponding coupled iCDW-rCDW free-energy expansions, with the rCDW order parameter N_i transforming as M_1^+, are once again identical to that written in Eq. (10), which promotes the mixed 3**Q**-3**Q** and 2**Q**-1**Q** configurations.

Similar to the cases studied above, the 2**Q**-1**Q** configuration breaks the threefold rotational symmetry of the kagome lattice by causing an orthorhombic distortion given by the order parameter $\boldsymbol{\eta}$ [see Eq. (19)]. On the other hand, the 3**Q**-3**Q** mixed configuration is accompanied by uniform magnetic order, whose order parameter μ transforms as either mM_1^- (i.e., time-reversal-odd A_{1u}), for symmetric interorbital iCDW order, or as mM_2^- (i.e., time-reversal-odd A_{2u}), for antisymmetric interorbital iCDW order. While the former corresponds to *magnetic monopolar* order, the latter is a *magnetic toroidal dipolar* order [87]. They have unique magnetoelectric properties, as described by the following Landau free-energy

couplings:

$$\mathcal{F}_{\text{mag}-\text{el}}^{(mM_1^-)} \sim \mu\, E_z B_z, \tag{24}$$

and

$$\mathcal{F}_{\text{mag}-\text{el}}^{(mM_2^-)} \sim \mu\, (\mathbf{E} \times \mathbf{B}) \cdot \hat{\mathbf{z}}. \tag{25}$$

We note that magnetic toroidal dipolar order has been previously proposed to explain the time-reversal symmetry-breaking state of the AV_3Sb_5 kagome compounds in Ref. [89]. Indeed, the resulting magnetic space group name associated with the 3**Q**-3**Q** configuration with mM_2^- iCDW order (see Table III) is the same as that discussed in Ref. [89]. The main difference is that, in our case, the toroidal moment is a subsidiary order of a triple-**Q** iCDW order that also breaks the translational symmetry of the crystal.

VII. CONCLUSIONS

We have combined phenomenology, DFT calculations, and group theory to derive the possible mixed iCDW-rCDW states of AV_3Sb_5 compounds that can arise from interactions involving the two pairs of occupied and unoccupied vHs closest to the Fermi level. Because these four vHs have different orbital and sublattice structures, as shown in Fig. 1, various types of rCDW and iCDW states are possible. Current experimental and first-principles results constrain the rCDW to transform as the M_1^+ irrep, which corresponds to intraorbital/intra-vHs order in our model. On the other hand, the available experimental data does not allow one to unambiguously identify the type of iCDW order that is possibly realized in AV_3Sb_5. Our findings, which are summarized in Table III, reveal seven different possible iCDW order parameters involving these two pairs of vHs. As we discussed here, any of these iCDW configurations must be accompanied by an SDW pattern that shares the same symmetry properties; in the particular case of intraorbital/intra-vHs iCDW, the magnetization density peaks at the Sb atoms, as shown in Fig. 7. We note that one of such iCDW orders (mM_2^+) was previously identified in Ref. [50], and that an alternative classification scheme was also put forward in Ref. [57].

One of our main results, derived from the analysis of the coupled iCDW-rCDW free-energy expansion, is that, unless the iCDW order is unidirectional, it will be accompanied by rCDW order, either in a 3**Q**-3**Q** or in a 2**Q**-1**Q** mixed configuration. The intrinsic coupling between these two types of order was previously discussed in Refs. [50,51]; here, we focused on the most favored minima of the full free energy in the large parameter space available.

Thus, because we identify seven types of iCDW order and two possible minima of the coupled free energy with the M_1^+ rCDW order, there are 14 different viable mixed iCDW-rCDW configurations, as shown in Table III. Although our list of seven iCDW orders was derived from the symmetry properties of the Bloch states at the four vHs, it is quite comprehensive, as there are only eight possible irreps for the iCDW order parameter with wave vector corresponding to the M point. The only irrep that did not appear in our analysis is mM_1^+. The reason for this absence is because this irrep is trivial in the sense that it breaks no symmetries other than the translational symmetry (due to its finite wave vector) and time-reversal symmetry. Thus, there is no combination of currents normal to the c axis that gives rise to an order parameter that transform as mM_1^+.

Our second main result is the identification of the experimental manifestations of these 14 different states. The formal assignment in terms of magnetic space groups is presented in the last column of Table III. While the seven 3**Q**-3**Q** phases have seven different magnetic space groups, the seven 2**Q**-1**Q** configurations group in just two different magnetic space groups. In principle, detailed x-ray and neutron scattering experiments may be able to distinguish between these magnetic space groups and thus identify which iCDW order is realized in AV_3Sb_5.

Conversely, these iCDW-rCDW mixed configurations display subsidiary uniform (i.e., zero wave vector) orders that can be identified experimentally, as discussed in Table III. In particular, while the 2**Q**-1**Q** phases have no uniform magnetic order, they all display an orthorhombic distortion that scales as the square of the iCDW order parameter, regardless of the type of iCDW order present. In contrast, each of the seven 3**Q**-3**Q** phases display different types of uniform magnetic order, whose order parameters scale as the cube of the iCDW order parameter. The simplest type of uniform magnetic order—ferromagnetism—is realized in the case of intraorbital/intra-vHs iCDW order. In all cases that involve inter-vHs order, a more exotic type of uniform magnetism arises, namely, magnetic octupolar, magnetic toroidal, and magnetic monopolar order. Each of them displays unique magnetostriction, magnetoelectric, or magnetoelectrostriction properties, which can be probed by the appropriate combinations of magnetic fields, electric fields, and in-plane uniaxial strain shown in the last column of Table III. Moreover, as we discussed above, if the iCDW order also breaks translational symmetry along the c axis, these uniform magnetic states become "antiferromagnetic," in the sense that they acquire modulation along the c axis

Our results therefore provide concrete guidance to experimentally establish the type of loop-current order realized in AV_3Sb_5. In this regard, we note that while experiments have reported threefold rotational symmetry breaking deep inside the charge-ordered phase of certain kagome metals [38,46,47,62,63], which seems consistent with the 2**Q**-1**Q** state, it is important to establish whether this symmetry breaking is a bulk or surface phenomenon, and whether it persists in the absence of applied magnetic fields, which could imply one of the 3**Q**-3**Q** states. Establishing the type of iCDW order realized in these compounds is important not only to identify the dominant interactions between the various vHs present near the Fermi level, but also to elucidate the properties of the superconducting state that onsets deep inside the charge-ordered phase.

Indeed, the type of subsidiary uniform order realized in the mixed iCDW-rCDW state can have profound consequences for the pairing state. For instance, the ferromagnetic moments generated in the 3**Q**-3**Q** intraorbital-iCDW state are expected to oppose pairing and thus strongly suppress conventional superconductivity. On the other hand, the orthorhombic distortion in the 2**Q**-1**Q** state can mix pairing states of different symmetries, and even induce nodes in a chiral superconducting state [21]. As for the higher-order magnetic multipolar

orders induced in the other 3**Q**-3**Q** states, little is known about their interplay with superconductivity. One interesting prospect is that the simultaneous presence of both electric and magnetic dipole moments may harbor the unusual pair-density wave (PDW) state [90]. Interestingly, a PDW was recently proposed to be realized in these compounds [19]. More broadly, the AV_3Sb_5 systems offer a promising framework to investigate and elucidate how pairing is modified by exotic types of uniform magnetic order.

ACKNOWLEDGMENTS

We acknowledge helpful discussions with M. I. Aroyo and M. Geier. M.H.C. has received funding from the European Union's Horizon 2020research and innovation programme under the Marie Sklodowska-Curie Grant Agreement No. 101024210. T.B. was supported by a NSF CAREER Grant No. DMR-2046020. B.M.A. acknowledges support from a research grant (40509) from VILLUM FONDEN. R.M.F. was supported by the Air Force Office of Scientific Research under Award No. FA9550-21-1-0423.

APPENDIX A: FIRST-PRINCIPLES METHODS

First-principles density functional theory (DFT) calculations were performed using the Vienna *ab initio* Simulation Package (VASP) [91,92]. Further details of the first-principles calculations were discussed in Ref. [54]. The band structure shown in Fig. 1(c) is that of CsV_3Sb_5. Since the effect of the alkali metal is mostly geometric in these systems, the band structure of KV_3Sb_5 and RbV_3Sb_5 are similar [9]. While it is possible that small energy shifts change the order of the vHs, this does not affect the present discussion.

The irreps of the DFT bands were obtained by using the Kohn-Sham band wave functions at the M point, and finding their transformation properties under space group by inspection. The resultant irreps and orbital characters were confirmed to be consistent with each other by using the induced band representations approach [93].

APPENDIX B: TRANSFORMATION PROPERTIES OF POSSIBLE ORDER PARAMETERS

In this section, we derive the transformation properties (and hence the irreps) corresponding to the different order parameters, by starting from the individual atomic orbitals of the V atoms and then building the Hermitian bilinears. For the sake of brevity, we only focus on the two bands that give rise to the vHs below the Fermi level, but the same procedure can be extended to include the ones above the Fermi level as well.

We consider ideal kagome layers stacked with atoms aligned on top of each other. This configuration gives rise to the space group $P6/mmm$, and corresponds to the crystal structure of AV_3Sb_5 compounds. The unit cell and the lattice vectors are shown in Fig. 1(a). There are three symmetry-equivalent V atoms in each unit cell. The $k_z = 0$ plane of the Brillouin zone is shown in Fig. 1(b). There are two bands near the Fermi level at the M points, which transform as M_1^+ and M_4^+ irreps of the space group. Note that we use the convention of the Cracknell-Davies-Miller-Love tables [85,86] available in the tables of the Bilbao Crystallographic Server, whereas another commonly used resource is the book of Koster [94]. The irreps of the little group of M in both conventions are shown in Table IV.

TABLE IV. Characters of the irreps of the little group of the M_1 point (similarly to Table I in the main text). We only list the characters for the three generators of the little group, and these irreps correspond to the space group irreps by the same name. Note that the space group irreps are three dimensional, because the star of M has three distinct wave vectors. The only ambiguity upon going from the little group irreps to the space group irreps is possible minus signs in the off-diagonal elements, which are trivial up to a coordinate transformation, and do not change the characters of the irreps. Time-reversal (TR) odd irreps (not shown) are denoted by a m prefix as $mM_i^{\mp}$.

CDML [85]	Koster [94]	2_{001}	2_{010}	$\bar{1}$
$M_1^{\mp}$	$M_1^{\mp}$	$+1$	$+1$	∓ 1
$M_2^{\mp}$	$M_3^{\mp}$	$+1$	-1	∓ 1
$M_3^{\mp}$	$M_4^{\mp}$	-1	$+1$	∓ 1
$M_4^{\mp}$	$M_2^{\mp}$	-1	-1	∓ 1

The M_1^+ and the M_4^+ bands near the Fermi level at M are formed by vanadium d_{z^2} and d_{xz} orbitals, respectively. These orbitals transform as the A_{1g} and B_{2g} (or B_{3g}, depending on the axis choice) irreps of the mmm site symmetry group of the V site (see Fig. 1). We denote the annihilation operator for the A_{1g} orbital on atom V_i in the unit cell at $R = m \cdot \vec{a} + n \cdot \vec{b}$ as $a_{i\sigma,(m,n)}$, where σ is the spin component along $\hat{z} \parallel \vec{c}$. By inspection, i.e., by considering the effect of different symmetry operations on the positions of the atoms and on the alignment of the orbitals, we find that

$$\begin{aligned}
\bar{1} a^{\dagger}_{1\sigma,(0,0)} \bar{1}^{-1} &= a^{\dagger}_{1\sigma,(0,1)}, \\
2_{001} a^{\dagger}_{1\sigma,(0,0)} 2^{-1}_{001} &= (\sigma i) a^{\dagger}_{1\sigma,(0,1)}, \\
2_{010} a^{\dagger}_{1\sigma,(0,0)} 2^{-1}_{010} &= (+i) a^{\dagger}_{1-\sigma,(0,0)}, \\
\\
\bar{1} a^{\dagger}_{2\sigma,(0,0)} \bar{1}^{-1} &= a^{\dagger}_{2\sigma,(-1,0)}, \\
2_{001} a^{\dagger}_{2\sigma,(0,0)} 2^{-1}_{001} &= (\sigma i) a^{\dagger}_{2\sigma,(-1,0)}, \\
2_{010} a^{\dagger}_{2\sigma,(0,0)} 2^{-1}_{010} &= (+i) a^{\dagger}_{3-\sigma,(0,0)}, \\
\\
\bar{1} a^{\dagger}_{3\sigma,(0,0)} \bar{1}^{-1} &= a^{\dagger}_{3\sigma,(1,1)}, \\
2_{001} a^{\dagger}_{3\sigma,(0,0)} 2^{-1}_{001} &= (\sigma i) a^{\dagger}_{3\sigma,(1,1)}, \\
2_{010} a^{\dagger}_{3\sigma,(0,0)} 2^{-1}_{010} &= (+i) a^{\dagger}_{2-\sigma,(0,0)},
\end{aligned} \tag{B1}$$

where the spin-1/2 nature of the electrons are taken into account so that rotations by π bring in a phase factor of $\mp i$. Similarly, we denote the annihilation operator for the B_{2g} orbital on atom V_i in the unit cell at $R = m \cdot \vec{a} + n \cdot \vec{b}$ as $b_{i\sigma,(m,n)}$. By inspection, we find that

$$\begin{aligned}
\bar{1} b^{\dagger}_{1\sigma,(0,0)} \bar{1}^{-1} &= b^{\dagger}_{1\sigma,(0,1)}, \\
2_{001} b^{\dagger}_{1\sigma,(0,0)} 2^{-1}_{001} &= (-\sigma i) b^{\dagger}_{1\sigma,(0,1)}, \\
2_{010} b^{\dagger}_{1\sigma,(0,0)} 2^{-1}_{010} &= (-i) b^{\dagger}_{1-\sigma,(0,0)},
\end{aligned}$$

$$\begin{aligned}
\bar{1} b^\dagger_{2\sigma,(0,0)} \bar{1}^{-1} &= b^\dagger_{2\sigma,(-1,0)},\\
2_{001} b^\dagger_{2\sigma,(0,0)} 2^{-1}_{001} &= (-\sigma i) b^\dagger_{2\sigma,(-1,0)},\\
2_{010} b^\dagger_{2\sigma,(0,0)} 2^{-1}_{010} &= (+i) b^\dagger_{3-\sigma,(0,0)},
\end{aligned} \tag{B2}$$

$$\begin{aligned}
\bar{1} b^\dagger_{3\sigma,0} \bar{1}^{-1} &= b^\dagger_{3\sigma,(1,1)},\\
2_{001} b^\dagger_{3\sigma,0} 2^{-1}_{001} &= (-\sigma i) b^\dagger_{3\sigma,(1,1)},\\
2_{010} b^\dagger_{3\sigma,0} 2^{-1}_{010} &= (+i) b^\dagger_{2-\sigma,(0,0)}.
\end{aligned}$$

Note that $a^\dagger$ and $b^\dagger$ are creation operators for atomic orbitals localized in real space. The momentum-space counterparts that create electrons on Bloch states with wave vector $\vec{q} = q_1\vec{a}^* + q_2\vec{b}^*$ are defined as

$$c^\dagger_{i\sigma\vec{q}} = \sum_{m,n} a^\dagger_{i\sigma(m,n)} \exp\{-i(q_1 m + q_2 n)\}, \tag{B3}$$

$$d^\dagger_{i\sigma\vec{q}} = \sum_{m,n} b^\dagger_{i\sigma(m,n)} \exp\{-i(q_1 m + q_2 n)\}. \tag{B4}$$

We focus solely on the $\mathbf{k} = \mathbf{Q}_1 = \mathbf{a}^*/2$ point in the Brillouin zone, and drop the $\vec{q}$ subscript in the c and d operators. The transformation properties of these momentum-space operators are

$$\begin{aligned}
\bar{1} c^\dagger_{1\sigma} \bar{1}^{-1} &= c^\dagger_{1\sigma},\\
2_{001} c^\dagger_{1\sigma} 2^{-1}_{001} &= (\sigma i) c^\dagger_{1\sigma},\\
2_{010} c^\dagger_{1\sigma} 2^{-1}_{010} &= (+i) c^\dagger_{1-\sigma},
\end{aligned}$$

$$\begin{aligned}
\bar{1} c^\dagger_{2\sigma} \bar{1}^{-1} &= -c^\dagger_{2\sigma},\\
2_{001} c^\dagger_{2\sigma} 2^{-1}_{001} &= (-\sigma i) c^\dagger_{2\sigma},\\
2_{010} c^\dagger_{2\sigma} 2^{-1}_{010} &= (+i) c^\dagger_{3,-\sigma},
\end{aligned} \tag{B5}$$

$$\begin{aligned}
\bar{1} c^\dagger_{3\sigma} \bar{1}^{-1} &= -c^\dagger_{3\sigma},\\
2_{001} c^\dagger_{3\sigma} 2^{-1}_{001} &= (-\sigma i) c^\dagger_{3\sigma},\\
2_{010} c^\dagger_{3\sigma} 2^{-1}_{010} &= (+i) c^\dagger_{2-\sigma},
\end{aligned}$$

as well as

$$\begin{aligned}
\bar{1} d^\dagger_{1\sigma} \bar{1}^{-1} &= d^\dagger_{1\sigma},\\
2_{001} d^\dagger_{1\sigma} 2^{-1}_{001} &= (-\sigma i) d^\dagger_{1\sigma},\\
2_{010} d^\dagger_{1\sigma} 2^{-1}_{010} &= (-i) d^\dagger_{1-\sigma},\\
\bar{1} d^\dagger_{2\sigma} \bar{1}^{-1} &= -d^\dagger_{2\sigma},\\
2_{001} d^\dagger_{2\sigma} 2^{-1}_{001} &= (\sigma i) d^\dagger_{2\sigma},\\
2_{010} d^\dagger_{2\sigma} 2^{-1}_{010} &= (+i) d^\dagger_{3-\sigma},\\
\bar{1} d^\dagger_{3\sigma} \bar{1}^{-1} &= -d^\dagger_{3\sigma},\\
2_{001} d^\dagger_{3\sigma} 2^{-1}_{001} &= (\sigma i) d^\dagger_{3\sigma},\\
2_{010} d^\dagger_{3\sigma} 2^{-1}_{010} &= (+i) d^\dagger_{2-\sigma},
\end{aligned} \tag{B6}$$

The transformation properties of the bilinears follow from these equations.

[1] I. Syôzi, Statistics of kagomé lattice, Prog. Theor. Phys. **6**, 306 (1951).

[2] N. J. Ghimire and I. I. Mazin, Topology and correlations on the kagome lattice, Nat. Mater. **19**, 137 (2020).

[3] H.-M. Guo and M. Franz, Topological insulator on the kagome lattice, Phys. Rev. B **80**, 113102 (2009).

[4] L. Ye, M. Kang, J. Liu, F. von Cube, C. R. Wicker, T. Suzuki, C. Jozwiak, A. Bostwick, E. Rotenberg, D. C. Bell *et al.*, Massive Dirac fermions in a ferromagnetic kagome metal, Nature (London) **555**, 638 (2018).

[5] M. Kang, L. Ye, S. Fang, J.-S. You, A. Levitan, M. Han, J. I. Facio, C. Jozwiak, A. Bostwick, E. Rotenberg *et al.*, Dirac fermions and flat bands in the ideal kagome metal FeSn, Nat. Mater. **19**, 163 (2020).

[6] Z. Lin, J.-H. Choi, Q. Zhang, W. Qin, S. Yi, P. Wang, L. Li, Y. Wang, H. Zhang, Z. Sun, L. Wei, S. Zhang, T. Guo, Q. Lu, J.-H. Cho, C. Zeng, and Z. Zhang, Flatbands and Emergent Ferromagnetic Ordering in Fe_3Sn_2 Kagome Lattices, Phys. Rev. Lett. **121**, 096401 (2018).

[7] W. R. Meier, M.-H. Du, S. Okamoto, N. Mohanta, A. F. May, M. A. McGuire, C. A. Bridges, G. D. Samolyuk, and B. C. Sales, Flat bands in the CoSn-type compounds, Phys. Rev. B **102**, 075148 (2020).

[8] M. Kang, S. Fang, J.-K. Kim, B. R. Ortiz, S. H. Ryu, J. Kim, J. Yoo, G. Sangiovanni, D. Di Sante, B.-G. Park *et al.*, Twofold van Hove singularity and origin of charge order in topological kagome superconductor CsV_3Sb_5, Nat. Phys. **18**, 301 (2022).

[9] B. R. Ortiz, L. C. Gomes, J. R. Morey, M. Winiarski, M. Bordelon, J. S. Mangum, I. W. H. Oswald, J. A. Rodriguez-Rivera, J. R. Neilson, S. D. Wilson, E. Ertekin, T. M. McQueen, and E. S. Toberer, New kagome prototype materials: Discovery of KV_3Sb_5, RbV_3Sb_5, and CsV_3Sb_5, Phys. Rev. Mater. **3**, 094407 (2019).

[10] B. R. Ortiz, S. M. L. Teicher, Y. Hu, J. L. Zuo, P. M. Sarte, E. C. Schueller, A. M. Milinda Abeykoon, M. J. Krogstad, S. Rosenkranz, R. Osborn, R. Seshadri, L. Balents, J. He, and S. D. Wilson, CsV_3Sb_5: A $\mathbb{Z}_2$ Topological Kagome Metal with a Superconducting Ground State, Phys. Rev. Lett. **125**, 247002 (2020).

[11] B. R. Ortiz, P. M. Sarte, E. M. Kenney, M. J. Graf, S. M. L. Teicher, R. Seshadri, and S. D. Wilson, Superconductivity in the $\mathbb{Z}_2$ kagome metal KV_3Sb_5, Phys. Rev. Mater. **5**, 034801 (2021).

[12] Q. Yin, Z. Tu, C. Gong, Y. Fu, S. Yan, and H. Lei, Superconductivity and normal-state properties of kagome metal RbV_3Sb_5 single crystals, Chin. Phys. Lett. **38**, 037403 (2021).

[13] K. Jiang, T. Wu, J.-X. Yin, Z. Wang, M. Zahid Hasan, S. D. Wilson, X. Chen, and J. Hu, Kagome superconductors AV_3Sb_5 (A = K, Rb, Cs), arXiv:2109.10809.

[14] M. H. Christensen and T. Birol, Electrons go loopy in a family of superconductors, Nature (London) **602**, 216 (2022).

[15] T. Neupert, M. M. Denner, J.-X. Yin, R. Thomale, and M. Z. Hasan, Charge order and superconductivity in kagome materials, Nat. Phys. **18**, 137 (2022).

[16] C. Mu, Q. Yin, Z. Tu, C. Gong, H. Lei, Z. Li, and J. Luo, S-wave superconductivity in kagome metal CsV_3Sb_5 revealed by $^{121/123}$Sb NQR and ^{51}V NMR measurements, Chin. Phys. Lett. **38**, 077402 (2021).

[17] W. Duan, Z. Nie, S. Luo, F. Yu, B. R. Ortiz, L. Yin, H. Su, F. Du, A. Wang, Y. Chen *et al.*, Nodeless superconductivity in the kagome metal CsV_3Sb_5, Sci. China Phys. Mech. Astron. **64**, 107462 (2021).

[18] H.-S. Xu, Y.-J. Yan, R. Yin, W. Xia, S. Fang, Z. Chen, Y. Li, W. Yang, Y. Guo, and D.-L. Feng, Multiband Superconductivity with Sign-Preserving Order Parameter in Kagome Superconductor CsV_3Sb_5, Phys. Rev. Lett. **127**, 187004 (2021).

[19] H. Chen, H. Yang, B. Hu, Z. Zhao, J. Yuan, Y. Xing, G. Qian, Z. Huang, G. Li, Y. Ye *et al.*, Roton pair density wave in a strong-coupling kagome superconductor, Nature (London) **599**, 222 (2021).

[20] M. Roppongi, K. Ishihara, Y. Tanaka, K. Ogawa, K. Okada, S. Liu, K. Mukasa, Y. Mizukami, Y. Uwatoko, R. Grasset *et al.*, Bulk evidence of anisotropic *s*-wave pairing with no sign change in the kagome superconductor CsV_3Sb_5, arXiv:2206.02580.

[21] Z. Guguchia, C. Mielke III, D. Das, R. Gupta, J. X. Yin, H. Liu, Q. Yin, M. H. Christensen, Z. Tu, C. Gong *et al.*, Tunable nodal kagome superconductivity in charge ordered RbV_3Sb_5, arXiv:2202.07713.

[22] C. C. Zhao, L. S. Wang, W. Xia, Q. W. Yin, J. M. Ni, Y. Y. Huang, C. P. Tu, Z. C. Tao, Z. J. Tu, C. S. Gong *et al.*, Nodal superconductivity and superconducting domes in the topological Kagome metal CsV_3Sb_5, arXiv:2102.08356.

[23] M. L. Kiesel, C. Platt, and R. Thomale, Unconventional Fermi Surface Instabilities in the Kagome Hubbard Model, Phys. Rev. Lett. **110**, 126405 (2013).

[24] W.-S. Wang, Z.-Z. Li, Y.-Y. Xiang, and Q.-H. Wang, Competing electronic orders on kagome lattices at van Hove filling, Phys. Rev. B **87**, 115135 (2013).

[25] X. Wu, T. Schwemmer, T. Müller, A. Consiglio, G. Sangiovanni, D. Di Sante, Y. Iqbal, W. Hanke, A. P. Schnyder, M. M. Denner, M. H. Fischer, T. Neupert, and R. Thomale, Nature of Unconventional Pairing in the Kagome Superconductors AV_3Sb_5 (A = K, Rb, Cs), Phys. Rev. Lett. **127**, 177001 (2021).

[26] C. Wen, X. Zhu, Z. Xiao, N. Hao, R. Mondaini, H. Guo, and S. Feng, Superconducting pairing symmetry in the kagome-lattice Hubbard model, Phys. Rev. B **105**, 075118 (2022).

[27] C. Mielke III, D. Das, J.-X. Yin, H. Liu, R. Gupta, Y.-X. Jiang, M. Medarde, X. Wu, H. C. Lei, J. Chang *et al.*, Time-reversal symmetry-breaking charge order in a kagome superconductor, Nature (London) **602**, 245 (2022).

[28] R. Khasanov, D. Das, R. Gupta, C. Mielke, M. Elender, Q. Yin, Z. Tu, C. Gong, H. Lei, E. T. Ritz, R. M. Fernandes, T. Birol, Z. Guguchia, and H. Luetkens, Time-reversal symmetry broken by charge order in CsV_3Sb_5, Phys. Rev. Res. **4**, 023244 (2022).

[29] R. Gupta, D. Das, C. Mielke III, E. Ritz, F. Hotz, Q. Yin, Z. Tu, C. Gong, H. Lei, T. Birol, R. M. Fernandes, Z. Guguchia, H. Luetkens, and R. Khasanov, Two types of charge order in the superconducting kagome material CsV_3Sb_5, arXiv:2203.05055.

[30] J. Ge, P. Wang, Y. Xing, Q. Yin, H. Lei, Z. Wang, and J. Wang, Discovery of charge-4e and charge-6e superconductivity in kagome superconductor CsV_3Sb_5, arXiv:2201.10352.

[31] Q. Stahl, D. Chen, T. Ritschel, C. Shekhar, E. Sadrollahi, M. C. Rahn, O. Ivashko, M. v. Zimmermann, C. Felser, and J. Geck, Temperature-driven reorganization of electronic order in CsV_3Sb_5, Phys. Rev. B **105**, 195136 (2022).

[32] F. H. Yu, D. H. Ma, W. Z. Zhuo, S. Q. Liu, X. K. Wen, B. Lei, J. J. Ying, and X. H. Chen, Unusual competition of superconductivity and charge-density-wave state in a compressed topological kagome metal, Nat. Commun. **12**, 3645 (2021).

[33] K. Y. Chen, N. N. Wang, Q. W. Yin, Y. H. Gu, K. Jiang, Z. J. Tu, C. S. Gong, Y. Uwatoko, J. P. Sun, H. C. Lei, J. P. Hu, and J.-G. Cheng, Double Superconducting Dome and Triple Enhancement of T_c in the Kagome Superconductor CsV_3Sb_5 under High Pressure, Phys. Rev. Lett. **126**, 247001 (2021).

[34] T. Qian, M. H. Christensen, C. Hu, A. Saha, B. M. Andersen, R. M. Fernandes, T. Birol, and N. Ni, Revealing the competition between charge density wave and superconductivity in CsV_3Sb_5 through uniaxial strain, Phys. Rev. B **104**, 144506 (2021).

[35] Y. M. Oey, B. R. Ortiz, F. Kaboudvand, J. Frassineti, E. Garcia, R. Cong, S. Sanna, V. F. Mitrović, R. Seshadri, and S. D. Wilson, Fermi level tuning and double-dome superconductivity in the kagome metal $CsV_3Sb_{5-x}Sn_x$, Phys. Rev. Mater. **6**, L041801 (2022).

[36] S.-Y. Yang, Y. Wang, B. R. Ortiz, D. Liu, J. Gayles, E. Derunova, R. Gonzalez-Hernandez, L. Šmejkal, Y. Chen, S. S. P. Parkin *et al.*, Giant, unconventional anomalous Hall effect in the metallic frustrated magnet candidate, KV_3Sb_5, Sci. Adv. **6**, eabb6003 (2020).

[37] Y.-X. Jiang, J.-X. Yin, M. M. Denner, N. Shumiya, B. R. Ortiz, G. Xu, Z. Guguchia, J. He, M. S. Hossain, X. Liu *et al.*, Unconventional chiral charge order in kagome superconductor KV_3Sb_5, Nat. Mater. **20**, 1353 (2021).

[38] Y. Xiang, Q. Li, Y. Li, W. Xie, H. Yang, Z. Wang, Y. Yao, and H.-H. Wen, Twofold symmetry of c-axis resistivity in topological kagome superconductor CsV_3Sb_5 with in-plane rotating magnetic field, Nat. Commun. **12**, 6727 (2021).

[39] N. Ratcliff, L. Hallett, B. R. Ortiz, S. D. Wilson, and J. W. Harter, Coherent phonon spectroscopy and interlayer modulation of charge density wave order in the kagome metal CsV_3Sb_5, Phys. Rev. Mater. **5**, L111801 (2021).

[40] E. Uykur, B. R. Ortiz, S. D. Wilson, M. Dressel, and A. A. Tsirlin, Optical detection of the density-wave instability in the kagome metal KV_3Sb_5, npj Quantum Mater. **7**, 16 (2022).

[41] B. R. Ortiz, S. M. L. Teicher, L. Kautzsch, P. M. Sarte, N. Ratcliff, J. Harter, J. P. C. Ruff, R. Seshadri, and S. D. Wilson, Fermi Surface Mapping and the Nature of Charge-Density-Wave Order in the Kagome Superconductor CsV_3Sb_5, Phys. Rev. X **11**, 041030 (2021).

[42] C. Li, X. Wu, H. Liu, C. Polley, Q. Guo, Y. Wang, X. Han, M. Dendzik, M. H. Berntsen, B. Thiagarajan, Y. Shi, A. P. Schnyder, and O. Tjernberg, Coexistence of two intertwined charge density waves in a kagome system, Phys. Rev. Res. **4**, 033072 (2022).

[43] R. Lou, A. Fedorov, Q. Yin, A. Kuibarov, Z. Tu, C. Gong, E. F. Schwier, B. Büchner, H. Lei, and S. Borisenko, Charge-Density-Wave-Induced Peak-Dip-Hump Structure and the Multiband Superconductivity in a Kagome Superconductor CsV_3Sb_5, Phys. Rev. Lett. **128**, 036402 (2022).

[44] H. Li, T. T. Zhang, T. Yilmaz, Y. Y. Pai, C. E. Marvinney, A. Said, Q. W. Yin, C. S. Gong, Z. J. Tu, E. Vescovo, C. S. Nelson, R. G. Moore, S. Murakami, H. C. Lei, H. N. Lee, B. J. Lawrie, and H. Miao, Observation of Unconventional Charge Density

Wave without Acoustic Phonon Anomaly in Kagome Superconductors AV_3Sb_5 (A = Rb, Cs), Phys. Rev. X **11**, 031050 (2021).

[45] H. Luo, Q. Gao, H. Liu, Y. Gu, D. Wu, C. Yi, J. Jia, S. Wu, X. Luo, Y. Xu *et al.*, Electronic nature of charge density wave and electron-phonon coupling in kagome superconductor KV_3Sb_5, Nat. Commun. **13**, 273 (2022).

[46] H. Li, H. Zhao, B. R. Ortiz, T. Park, M. Ye, L. Balents, Z. Wang, S. D. Wilson, and I. Zeljkovic, Rotation symmetry breaking in the normal state of a kagome superconductor KV_3Sb_5, Nat. Phys. **18**, 265 (2022).

[47] L. Nie, K. Sun, W. Ma, D. Song, L. Zheng, Z. Liang, P. Wu, F. Yu, J. Li, M. Shan *et al.*, Charge-density-wave-driven electronic nematicity in a kagome superconductor, Nature (London) **604**, 59 (2022).

[48] S. Wu, B. R. Ortiz, H. Tan, S. D. Wilson, B. Yan, T. Birol, and G. Blumberg, Charge density wave order in the kagome metal AV_3Sb_5(A = Cs, Rb, K), Phys. Rev. B **105**, 155106 (2022).

[49] L. Yu, C. Wang, Y. Zhang, M. Sander, S. Ni, Z. Lu, S. Ma, Z. Wang, Z. Zhao, H. Chen, K. Jiang, Y. Zhang, H. Yang, F. Zhou, X. Dong, S. L. Johnson, M. J. Graf, J. Hu, H.-J. Gao, and Z. Zhao, Evidence of a hidden flux phase in the topological kagome metal CsV_3Sb_5, arXiv:2107.10714.

[50] T. Park, M. Ye, and L. Balents, Electronic instabilities of kagome metals: Saddle points and Landau theory, Phys. Rev. B **104**, 035142 (2021).

[51] Y.-P. Lin and R. M. Nandkishore, Complex charge density waves at van Hove singularity on hexagonal lattices: Haldane-model phase diagram and potential realization in the kagome metals AV_3Sb_5 (A = K, Rb, Cs), Phys. Rev. B **104**, 045122 (2021).

[52] M. M. Denner, R. Thomale, and T. Neupert, Analysis of Charge Order in the Kagome Metal AV_3Sb_5 (A = K, Rb, Cs), Phys. Rev. Lett. **127**, 217601 (2021).

[53] H. Tan, Y. Liu, Z. Wang, and B. Yan, Charge Density Waves and Electronic Properties of Superconducting Kagome Metals, Phys. Rev. Lett. **127**, 046401 (2021).

[54] M. H. Christensen, T. Birol, B. M. Andersen, and R. M. Fernandes, Theory of the charge density wave in AV_3Sb_5 kagome metals, Phys. Rev. B **104**, 214513 (2021).

[55] X. Feng, K. Jiang, Z. Wang, and J. Hu, Chiral flux phase in the Kagome superconductor AV_3Sb_5, Sci. Bull. **66**, 1384 (2021).

[56] C. Setty, H. Hu, L. Chen, and Q. Si, Electron correlations and T-breaking density wave order in a $\mathbb{Z}_2$ kagome metal, arXiv:2204.10116.

[57] X. Feng, Y. Zhang, K. Jiang, and J. Hu, Low-energy effective theory and symmetry classification of flux phases on the kagome lattice, Phys. Rev. B **104**, 165136 (2021).

[58] S. Zhou and Z. Wang, Chern Fermi-pockets and chiral topological pair density waves in kagome superconductors, arXiv:2110.06266.

[59] R. Tazai, Y. Yamakawa, S. Onari, and H. Kontani, Mechanism of exotic density-wave and beyond-Migdal unconventional superconductivity in kagome metal AV_3Sb_5 (A = K, Rb, Cs), Sci. Adv. **8**, eabl4108 (2022).

[60] A. Subedi, Hexagonal-to-base-centered-orthorhombic $4Q$ charge density wave order in kagome metals KV_3Sb_5, RbV_3Sb_5, and CsV_3Sb_5, Phys. Rev. Mater. **6**, 015001 (2022).

[61] H. Li, G. Fabbris, A. H. Said, Y. Y. Pai, Q. W. Yin, C. S. Gong, Z. J. Tu, H. C. Lei, J. P. Sun, J. G. Cheng *et al.*, Conjoined Charge Density Waves in the Kagome Superconductor CsV_3Sb_5, arXiv:2202.13530.

[62] H. Zhao, H. Li, B. R. Ortiz, S. M. L. Teicher, T. Park, M. Ye, Z. Wang, L. Balents, S. D. Wilson, and I. Zeljkovic, Cascade of correlated electron states in the kagome superconductor CsV_3Sb_5, Nature (London) **599**, 216 (2021).

[63] Y. Xu, Z. Ni, Y. Liu, B. R. Ortiz, S. D. Wilson, B. Yan, L. Balents, and L. Wu, Universal three-state nematicity and magneto-optical Kerr effect in the charge density waves in AV_3Sb_5 (A=Cs, Rb, K), arXiv:2204.10116.

[64] J. A. Wilson, F. J. D. Salvo, and S. Mahajan, Charge-density waves and superlattices in the metallic layered transition metal dichalcogenides, Adv. Phys. **24**, 117 (1975).

[65] F. J. Di Salvo and T. M. Rice, Charge-density waves in transition-metal compounds, Phys. Today **32**, 32 (1979).

[66] K. Rossnagel, On the origin of charge-density waves in select layered transition-metal dichalcogenides, J. Phys.: Condens. Matter **23**, 213001 (2011).

[67] H. H. Huang, X. Fan, D. J. Singh, and W. T. Zheng, Recent progress of TMD nanomaterials: Phase transitions and applications, Nanoscale **12**, 1247 (2020).

[68] Y. Hu, S. Yamane, G. Mattoni, K. Yada, K. Obata, Y. Li, Y. Yao, Z. Wang, J. Wang, C. Farhang, J. Xia, Y. Maeno, and S. Yonezawa, Time-reversal symmetry breaking in charge density wave of CsV_3Sb_5 detected by polar Kerr effect, arXiv:2208.08036.

[69] C. M. Varma, Non-Fermi-liquid states and pairing instability of a general model of copper oxide metals, Phys. Rev. B **55**, 14554 (1997).

[70] C. Nayak, Density-wave states of nonzero angular momentum, Phys. Rev. B **62**, 4880 (2000).

[71] F. D. M. Haldane, Model for a Quantum Hall Effect without Landau Levels: Condensed-Matter Realization of the "Parity Anomaly", Phys. Rev. Lett. **61**, 2015 (1988).

[72] J. Kang and Z. Tešanović, Theory of the valley-density wave and hidden order in iron pnictides, Phys. Rev. B **83**, 020505(R) (2011).

[73] A. V. Chubukov, R. M. Fernandes, and J. Schmalian, Origin of nematic order in FeSe, Phys. Rev. B **91**, 201105(R) (2015).

[74] C. Guo, C. Putzke, S. Konyzheva, X. Huang, M. Gutierrez-Amigo, I. Errea, D. Chen, M. G. Vergniory, C. Felser, M. H. Fischer *et al.*, Field-tuned chiral transport in charge-ordered CsV_3Sb_5, arXiv:2203.09593.

[75] M. L. Kiesel and R. Thomale, Sublattice interference in the kagome Hubbard model, Phys. Rev. B **86**, 121105 (2012).

[76] M. Klug, J. Kang, R. M. Fernandes, and J. Schmalian, Orbital loop currents in iron-based superconductors, Phys. Rev. B **97**, 155130 (2018).

[77] Y. Gu, Y. Zhang, X. Feng, K. Jiang, and J. Hu, Gapless excitations inside the fully gapped kagome superconductors AV_3Sb_5, Phys. Rev. B **105**, L100502 (2022).

[78] M. Y. Jeong, H.-J. Yang, H. S. Kim, Y. B. Kim, S. B. Lee, and M. J. Han, Crucial role of out-of-plane Sb p orbitals in Van Hove singularity formation and electronic correlations in the superconducting kagome metal CsV_3Sb_5, Phys. Rev. B **105**, 235145 (2022).

[79] Y. Hu, X. Wu, B. R. Ortiz, S. Ju, X. Han, J. Ma, N. C. Plumb, M. Radovic, R. Thomale, S. D. Wilson, A. P. Schnyder, and

M. Shi, Rich nature of Van Hove singularities in Kagome superconductor CsV_3Sb_5, Nat. Commun. **13**, 2220 (2022).

[80] L. Elcoro, B. Bradlyn, Z. Wang, M. G. Vergniory, J. Cano, C. Felser, B. A. Bernevig, D. Orobengoa, G. de la Flor, and M. I. Aroyo, Double crystallographic groups and their representations on the Bilbao Crystallographic Server, J. Appl. Crystallogr. **50**, 1457 (2017).

[81] E. M. Kenney, B. R. Ortiz, C. Wang, S. D. Wilson, and M. J. Graf, Absence of local moments in the kagome metal KV_3Sb_5 as determined by muon spin spectroscopy, J. Phys.: Condens. Matter **33**, 235801 (2021).

[82] D. M. Hatch and H. T. Stokes, *INVARIANTS*: Program for obtaining a list of invariant polynomials of the order-parameter components associated with irreducible representations of a space group, J. Appl. Crystallogr. **36**, 951 (2003).

[83] H. T. Stokes, D. M. Hatch, and B. J. Campbell, INVARIANTS, ISOTROPY Software Suite, iso.byu.edu.

[84] T. Bradley, C. Bradley, and A. Cracknell, *The Mathematical Theory of Symmetry in Solids: Representation Theory for Point Groups and Space Groups* (Clarendon Press, Oxford, 1972).

[85] A. Cracknell, S. Miller, B. Davies, and W. Love, *Kronecker Product Tables: In Four Volumes*, Kronecker Product Tables (Springer US, New York, 1979).

[86] M. I. Aroyo, A. Kirov, C. Capillas, J. M. Perez-Mato, and H. Wondratschek, Bilbao Crystallographic Server. II. Representations of crystallographic point groups and space groups, Acta Crystallogr. Sect. A **62**, 115 (2006).

[87] S. Hayami, M. Yatsushiro, Y. Yanagi, and H. Kusunose, Classification of atomic-scale multipoles under crystallographic point groups and application to linear response tensors, Phys. Rev. B **98**, 165110 (2018).

[88] Q. Xiao, Y. Lin, Q. Li, W. Xia, X. Zheng, S. Zhang, Y. Guo, J. Feng, and Y. Peng, Coexistence of multiple stacking charge density waves in kagome superconductor CsV_3Sb_5, arXiv:2201.05211.

[89] V. Scagnoli, D. D. Khalyavin, and S. W. Lovesey, Hidden magnetic order on a kagome lattice for KV_3Sb_5, Phys. Rev. B **106**, 064419 (2022).

[90] D. Agterberg, Novel magnetic field effects in unconventional superconductors, Physica C **387**, 13 (2003).

[91] G. Kresse and D. Joubert, From ultrasoft pseudopotentials to the projector augmented-wave method, Phys. Rev. B **59**, 1758 (1999).

[92] G. Kresse and J. Hafner, *Ab initio* molecular dynamics for liquid metals, Phys. Rev. B **47**, 558 (1993).

[93] B. Bradlyn, L. Elcoro, J. Cano, M. G. Vergniory, Z. Wang, C. Felser, M. I. Aroyo, and B. A. Bernevig, Topological quantum chemistry, Nature (London) **547**, 298 (2017).

[94] G. Koster, J. Dimmock, R. Wheeler, and H. Statz, *Properties of the Thirty-two Point Groups*, M.I.T. Press research monographs (M.I.T. Press, Cambridge, 1963).